Supergap and subgap enhanced currents in asymmetric S_1FS_2 Josephson junctions

Mohammad Alidoust[1] and Klaus Halterman[2]
[1]*Department of Physics, Norwegian University of Science and Technology, N-7491 Trondheim, Norway*
[2]*Michelson Lab, Physics Division, Naval Air Warfare Center, China Lake, California 93555, USA*

(Received 17 August 2020; revised 1 October 2020; accepted 17 November 2020; published 7 December 2020)

We have theoretically studied the supercurrent profiles in three-dimensional normal metal and ferromagnetic Josephson configurations, where the magnitude of the superconducting gaps in the superconducting leads are unequal, i.e., $\Delta_1 \neq \Delta_2$, creating asymmetric S_1NS_2 and S_1FS_2 systems. Our results reveal that by increasing the ratio of the superconducting gaps Δ_2/Δ_1, the critical supercurrent in a ballistic S_1NS_2 system can be enhanced by more than 100% and reaches a saturation point, or decays away, depending on the junction thickness, magnetization strength, and chemical potential. The total critical current in a diffusive S_1NS_2 system was found to be enhanced by more than 50% parabolically and reaches saturation by increasing one of the superconducting gaps. In a uniform ferromagnetic junction, the supercurrent undergoes reversal by increasing $\Delta_2/\Delta_1 > 1$. Through decomposing the total supercurrent into its supergap and subgap components, our results illustrate their crucial relative contributions to the Josephson current flow. It was found that the competition of subgap and supergap currents in a S_1FS_2 junction results in the emergence of second harmonics in the current-phase relation. In contrast to a diffusive asymmetric Josephson configuration, the behavior of the supercurrent in a ballistic system with $\Delta_2/\Delta_1 = 1$ can be properly described by the subgap current component only, in a wide range of parameter sets, including Fermi level mismatch, magnetization strength, and junction thickness. Interestingly, when $\Delta_2/\Delta_1 > 1$, our results have found multiple parameter sets where the total supercurrent is driven by the supergap component. Therefore, our comprehensive study highlights the importance of subgap and supergap supercurrent components in both the ballistic and diffusive regimes. We focus on experimentally accessible material and geometric parameters that can lead to advancements in cryogenic devices based on Josephson junction architectures that utilize supergap currents, which are less sensitive to temperature compared to the subgap current.

DOI: 10.1103/PhysRevB.102.224504

I. INTRODUCTION

When two superconductors with different macroscopic phases are weakly coupled by proximity effects, a finite dissipationless current can flow, demonstrating the Josephson effect [1]. The current flow is carried through the coherent tunneling of Cooper pairs from one superconductor (S) to the other. The coherent nature of Cooper pairs allows for supercurrent flow through finite-thickness normal (N) metal and ferromagnetic (F) materials (SNS and SFS junctions). For these types of junctions, the physical quantities of interest can have complicated variations across the structure over a wide range of length scales due to proximity induced inhomogeneous superconductivity.

The widely accepted microscopic theory of conventional superconductors is the mean-field BCS theory, where two electrons with opposite momenta and spins create a single boson through lattice vibrations. This theory was later reformulated by introducing particle-hole space, which is the well-known Bogoliubov-de Gennes (BdG) approach [2]. To microscopically study systems containing a superconducting segment, one employs the associated BdG Hamiltonian with pair potential $\Delta(x)$ to account for the spatially varying superconducting correlations. The competition between superconducting order and other phases in proximity coupled junctions can induce striking phenomena that has attracted considerable attention over the decades [3–30]. Differing approaches and a wide range of approximations have been incorporated to study various normal and ferromagnetic superconducting hybrids that have achieved success to describe experimental observations [31–44]. For instance, a recent study of superconducting (half-)metallic spin valves has shown good agreement between theoretical predictions and experimental observations [45–48].

Nevertheless, except in simple situations, it is highly challenging to obtain analytical solutions to the BdG Hamiltonian. One particular example is asymmetric Josephson junctions, where the pair potentials in the S regions are different, i.e., $\Delta_1 \neq \Delta_2$. There are mainly two approaches for studying current flow in S_1NS_2 and S_1FS_2 configurations. (i) The wave function approach, where one diagonalizes the BdG Hamiltonian to obtain the wave functions and energies, which after application of the appropriate boundary conditions, permits calculation of the subgap bound states. To further simplify the resultant expressions, the vast majority of works utilize the so-called Andreev approximation. (ii) The other approach is Gorkov's Green function technique [49]. Here, one needs to incorporate multiple simplifying assumptions for obtaining simple and solvable equations. The best-known approximation in this approach is the quasiclassical approximation where the Fermi energy is considered the largest energy in the system, leading to the Eilenberger equation [50]. One

main advantage of this approach is that it can conveniently accommodate nonmagnetic impurities via a white-noise scattering potential. In the presence of disorder and nonmagnetic impurities one can integrate the Eilenberger equation over the random quasiparticle scattering angle to arrive at the Usadel equation [51]. This approach has been recently generalized to a spin-orbit-coupled electron gas to study several phenomena including: the spatial distribution of spin currents [52,53], also generalized to the surface state of three-dimensional topological insulators [54,55], Weyl semimetals [56], and black phosphorus [57].

The former approach (i) has been used to simulate ballistic systems, where multiple interference effects from the propagating quasiparticles strongly influences the transport behavior of the system. It was demonstrated that this approach, if followed analytically, can be problematic for asymmetric S_1NS_2 junctions even within the quasiclassical regime [58]. The problem becomes increasingly difficult in asymmetric S_1FS_2 structures due to the inclusion of band spin splitting. One main issue is to properly obtain the contribution of supergap channels to the total supercurrent. These modes become particularly important in asymmetric junctions [39,55,58,59] due to the imbalance of superconducting gaps that open up the continuum domain to states that can carry considerable amounts of supercurrent.

In this paper, we aim to study the behavior of the supercurrent in asymmetric three-dimensional S_1NS_2 and S_1FS_2 Josephson junctions in both the ballistic and diffusive regimes. Due to the asymmetry in the pair potential "well," three relevant energy scales play a role in the net supercurrent response: (i) subgap energies ($\varepsilon \leqslant \Delta_1$), which comprise the resonant Andreev bound states, (ii) supergap energies ($\Delta_1 < \varepsilon \leqslant \Delta_2$), and (iii) energies in the continuum, where $\varepsilon > \Delta_2$. We demonstrate that our microscopic numerical approaches in the ballistic regime can adequately describe the supercurrent flow in all three energy regimes and provides an accessible framework that recovers previous results in various asymptotic limits for a simpler one-dimensional quasiclassical S_1NS_2 system [58]. Our numerical approaches allow for exploring realms beyond those studied in the vast majority of the literature without imposing any limitations to Fermi level mismatch and magnetization strength (supporting weak magnetization to a half-metallic phase). Our results reveal that when $\Delta_2/\Delta_1 = 1$, the subgap component of the supercurrent that describes the resonant bound states can properly account for the total supercurrent in a ballistic Josephson junction, regardless of Fermi level mismatch, junction thickness, and magnetization strength. When $\Delta_2/\Delta_1 > 1$, we find the the critical current can be strongly enhanced in highly asymmetric ballistic S_1NS_2 junctions. By means of the current-phase relations, we find that the supergap and subgap supercurrent components can propagate in opposite directions, and within certain regimes, the subgap supercurrent vanishes, so that the total supercurrent arises from supergap states.

In the full proximity limit of the diffusive regime, we find that the critical supercurrent can be enhanced by more than 50% when increasing the superconducting gap ratio to $\Delta_2/\Delta_1 \sim 10$, in an asymmetric S_1NS_2 junction. The critical supercurrent also shows an oscillatory behavior in S_1FS_2 junctions when increasing the exchange field intensity, and additionally, the supercurrent undergoes reversals as a function of Δ_2/Δ_1 for certain magnetization strengths. By calculating the total current-phase relation with its subgap and supergap current components, our results reveal that the emergence of a $\sin 2\Delta\varphi$ harmonic close to a current reversal point is the consequence of the intricate competition between the subgap and supergap currents flowing in opposite directions.

The paper is organized as follows: In Sec. II, we have summarized the main equations which establish the theoretical framework employed throughout the calculations. In Secs. II A and II B, we present detailed formulations of the ballistic and diffusive regimes, respectively. In Sec. III, the main results and findings are presented. In Secs. III A and III B, we discuss the results for the ballistic and diffusive regimes, respectively. Lastly, in Sec. IV, we give concluding remarks.

II. THEORY AND MODEL

In the ballistic regime, we directly solve the microscopic Bogoliubov-de Gennes (BdG) equations [2]. In Appendix A we also outline a complementary numerical method that can be employed to contrast and compare results. By employing two distinct numerical approaches [34–37,60,61], it allows for a comprehensive and accurate investigation into general hybrid Josephson junctions without being limited to a narrow range of ferromagnetic exchange fields and Fermi level differences. Moreover, both approaches produce similar results, as expected. In other words, with these methods in the ballistic regime, one is able to consider a wide parameter space from weak magnetizations to half-metallic systems [37,45,46,48], over a wide range of Fermi level mismatches between the S electrodes and junction insert. Of course, limiting cases such as the quasiclassical regime can be studied as well [35,56,57,61,62]. For systems containing impurities and disorder, we make use of the Usadel equation [51] in the full proximity limit of the quasiclassical regime to study the diffusive motion of quasiparticles in asymmetric S_1NS_2 and S_1FS_2 systems.

A. Ballistic regime

The effective Hamiltonian that describes our asymmetric Josephson junction is given by:

$$\begin{aligned}\mathcal{H}_{\rm eff} = \int d^3r \Bigg\{ & \sum_s \psi_s^\dagger(\boldsymbol{r})\mathcal{H}_0\psi_s(\boldsymbol{r}) \\ & + \frac{1}{2}\Bigg[\sum_{s\,s'}(i\sigma_y)_{ss'}\Delta(\boldsymbol{r})\psi_s^\dagger(\boldsymbol{r})\psi_{s'}^\dagger(\boldsymbol{r}) + \text{H.c.}\Bigg] \\ & - \sum_{s\,s'}\psi_s^\dagger(\boldsymbol{r})(\mathbf{h}\cdot\boldsymbol{\sigma})_{ss'}\psi_{s'}(\boldsymbol{r})\Bigg\}, \end{aligned} \tag{1}$$

where s, s' are spin indices, $\boldsymbol{\sigma}$ are Pauli matrices, and the exchange energy $\mathbf{h}$ describes the ferromagnet exchange interaction. We consider inhomogeneous systems where spatial variations occur in the x-direction. Thus, the kinetic part of

the single particle Hamiltonian is defined as

$$\mathcal{H}_0(x) = -\frac{1}{2m}\frac{\partial^2}{\partial x^2} + \varepsilon_\perp - E_F(x), \tag{2}$$

in which $\varepsilon_\perp = \frac{1}{2m}(k_y^2 + k_z^2)$ is the quasiparticle energy in the yz plane of Fig. 1. To accommodate the possibility of differing bandwidths in the two junction materials, we take the Fermi level $E_F(x)$ to equal E_{FM} in the ferromagnet region and E_{FS} in the superconductor region. Following standard procedures [2], we then utilize the generalized Bogoliubov transformation, $\psi_s = \sum_n (u_{ns}\gamma_n + \eta_s v_{ns}^*\gamma_n^\dagger)$, where $\eta_s \equiv 1(-1)$ for spin-down (up), to cast Eq. (1) in terms of the spin-generalized BdG equations [2]:

$$\begin{pmatrix} \mathcal{H}_0 - h_z & -h_x + ih_y & 0 & \Delta \\ -h_x - ih_y & \mathcal{H}_0 + h_z & \Delta & 0 \\ 0 & \Delta^* & -(\mathcal{H}_0 - h_z) & -h_x + ih_y \\ \Delta^* & 0 & -h_x - ih_y & -(\mathcal{H}_0 + h_z) \end{pmatrix} \begin{pmatrix} u_{n\uparrow}(x) \\ u_{n\downarrow}(x) \\ v_{n\uparrow}(x) \\ v_{n\downarrow}(x) \end{pmatrix} = \epsilon_n \begin{pmatrix} u_{n\uparrow}(x) \\ u_{n\downarrow}(x) \\ v_{n\uparrow}(x) \\ v_{n\downarrow}(x) \end{pmatrix}, \tag{3}$$

where u_{ns} and v_{ns} are the quasiparticle and quasihole amplitudes, respectively (for $s = \uparrow, \downarrow$). The generalized BdG technique has been shown to provide a numerically stable framework for solving inhomogeneous superconductivity problems [36,46,48,60]. For the layered Josephson junctions [9] considered in this work, we assume each F and S layer is infinite in the yz plane and the finite layer thicknesses extend along the x axis (see Fig. 1). As a result, the BdG equations are translationally invariant in the yz plane and become quasi-one-dimensional in x.

To solve the BdG equation, we first expand [36,60] the quasiparticle amplitudes in a Fourier series using a complete set of N basis functions:

$$\psi_n(x) = \sqrt{\frac{2}{d}}\sum_{q=0}^{N} \sin(k_q x)\hat{\psi}_q(k_q), \tag{4}$$

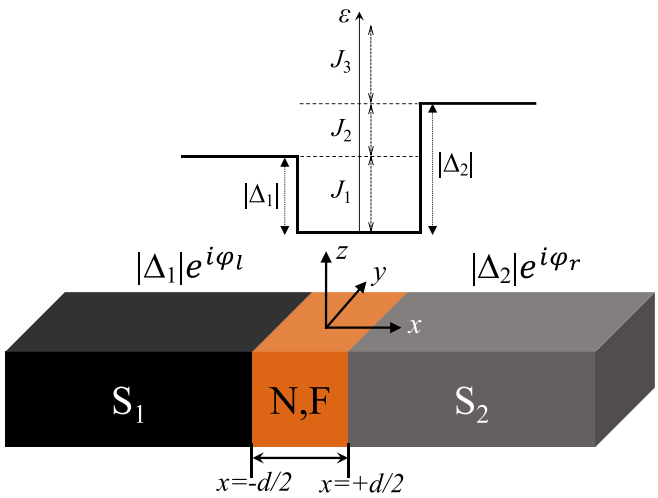

FIG. 1. Schematic of the asymmetric Josephson junction. The left and right superconductors have different superconducting gaps, $\Delta_{1,2}$, and macroscopic phases, $\varphi_{l,r}$, respectively. The superconductor-nonsuperconductor interfaces are located at $x = \pm d/2$. The two superconductors are connected either by a normal metal (N) or ferromagnet (F), making S_1NS_2 and S_1FS_2 Josephson configurations. The subgap and supergap currents are marked by J_1 and $J_{2,3}$, respectively, depending on the quasiparticle energy ε. The superconducting phase difference is defined by $\Delta\varphi = |\varphi_l - \varphi_r|$.

where $\psi_n(x) = (u_{n\uparrow}(x), u_{n\downarrow}(x), v_{n\uparrow}(x), v_{n\downarrow}(x))$, and $\hat{\psi}_q = (\hat{u}_{q\uparrow}, \hat{u}_{q\downarrow}, \hat{v}_{q\uparrow}, \hat{v}_{q\downarrow})$. The wave vector $k_q = q\pi/d$ is discretized by the thickness of junction d. Next, we transform the real-space BdG equations by first inserting Eq. (4) into Eq. (3) and using orthogonality of the basis set to give:

$$\hat{H}_0(q, q') = \frac{2}{d}\int_0^d dx \left\{ \left(\frac{k_q^2}{2m} + \varepsilon_\perp - E_F(x) \right) \times \sin(k_q x)\sin(k_{q'} x) \right\}, \tag{5a}$$

$$\hat{\Delta}(q, q') = \frac{2}{d}\int_0^d dx \Delta(x)\sin(k_q x)\sin(k_{q'} x), \tag{5b}$$

and

$$\hat{h}_i(q, q') = \frac{2}{d}\int_0^d dx\, h_i(x)\sin(k_q x)\sin(k_{q'} x). \tag{5c}$$

Here $i = x, y, z$ and we have defined $\hat{u}_\sigma = (\hat{u}_{1\sigma}, \hat{u}_{2\sigma}, \ldots, \hat{u}_{N\sigma})$, $\hat{v}_\sigma = (\hat{v}_{1\sigma}, \hat{v}_{2\sigma}, \ldots, \hat{v}_{N\sigma})$. Additional details on this solution process can be found elsewhere [10].

To compute the dc Josephson current, we numerically diagonalize the Fourier transformed BdG equations [with matrix elements in Eqs. (5a)–(5c)] to get the eigenenergies ϵ_n and quasiparticle coefficients $u_{i\sigma}$, $v_{i\sigma}$ $(i = 1, \ldots, N)$. The real-space amplitudes are then obtained via the series expansion in Eq. (4). Since we wish to determine the current-phase relation for asymmetric Josephson junctions, the input for the pair potential is taken to be the bulk gap, $\Delta_1 \exp(i\varphi_l)$ in S_1 and $\Delta_2 \exp(i\varphi_r)$ in S_2. With this form for $\Delta(x)$, and making use of the obtained wave functions and eigenenergies, we calculate the charge current with the expression,

$$J_x = \frac{2e}{m}\sum_{ns} \mathrm{Im}\left[u_{ns}\frac{\partial u_{ns}^*}{\partial x} f_n + v_{ns}\frac{\partial v_{ns}^*}{\partial x}(1 - f_n) \right], \tag{6}$$

where f_n is the Fermi function. The supercurrent satisfies the conservation law

$$\frac{\partial J_x(x)}{\partial x} = 2e\,\mathrm{Im}\left\{ \Delta(x)\sum_n [u_{n\uparrow}^* v_{n\downarrow} + u_{n\downarrow}^* v_{n\uparrow}] \tanh\left(\frac{\epsilon_n}{2T}\right) \right\}. \tag{7}$$

Thus, within the junction region where $\Delta(x)$ vanishes, the current density is uniform. We refer the reader to Refs. [36,60]

for further details on the methods used here for calculating the supercurrent. Also, an alternative approach to study ballistic asymmetric S_1NS_2 and S_1FS_2 systems is described in Appendix A.

B. Diffusive regime

In a system containing nonmagnetic impurities and disorder, the motion of quasiparticles can be described by a diffusion equation because of the scattering sources. In the quasiclassical regime, where the Fermi energy is the largest energy scale in the system, the diffusion equation is given by the Usadel equation [51],

$$D\hat{\nabla}\{\hat{G}(\varepsilon,\mathbf{r})\hat{\nabla}\hat{G}(\varepsilon,\mathbf{r})\}+i[\varepsilon\hat{\rho}_z,\hat{G}(\varepsilon,\mathbf{r})]=0, \tag{8a}$$

$$\hat{G}(\varepsilon,\mathbf{r})=\begin{pmatrix}G^A & G^K\\ 0 & G^R\end{pmatrix}, \tag{8b}$$

where D is the diffusion constant, $\hat{\nabla}\equiv(\partial_x,\partial_y,\partial_z)$, $\mathbf{r}=(x,y,z)$, and the quasiparticle energy ε is measured relative to the Fermi level. The total Green's function $\hat{G}(\varepsilon,\mathbf{r})$ is comprised of the advanced $G^A(\varepsilon,\mathbf{r})$, retarded $G^R(\varepsilon,\mathbf{r})$, and Keldysh $G^K(\varepsilon,\mathbf{r})$ propagators. The 4×4 Pauli matrices in Nambu space are given by $\hat{\rho}_z=\tau_z\sigma_0$ and $\hat{\rho}_0=\tau_0\sigma_0$, in which τ_i and σ_i are 2×2 Pauli matrices in particle-hole and spin spaces, respectively. Throughout the following calculations, an equilibrium state is considered so that the retarded and Keldysh components of the total Green's function can be obtained from the advanced component by symmetry considerations. For example, $G^A(\varepsilon,\mathbf{r})=-\{\hat{\rho}_zG^R(\varepsilon,\mathbf{r})\hat{\rho}_z\}^\dagger$ and $G^K(\varepsilon,\mathbf{r})=\{G^R(\varepsilon,\mathbf{r})-G^A(\varepsilon,\mathbf{r})\}\tanh(\varepsilon k_BT/2)$, where k_B is the Boltzmann constant, and the system temperature is denoted by T. To simulate the asymmetric Josephson junction shown in Fig. 1, we assume that the superconducting leads are tunnel coupled to the ferromagnetic region and can be described by [63]:

$$\zeta\hat{G}\mathbf{n}\cdot\hat{\nabla}\hat{G}=[\hat{G},\hat{G}_S],\quad G^R_S=\begin{pmatrix}\mathcal{C} & \mathcal{S}e^{+i\varphi}\\ \mathcal{S}e^{-i\varphi} & -\mathcal{C}\end{pmatrix}. \tag{9}$$

Here ζ is the ratio of the barrier resistance to the resistivity of the normal layer, and $\mathbf{n}$ is the unit vector normal to the interfaces. The retarded component of the total Green's function inside a superconducting lead can be expressed by $\hat{G}_S$ so that $\mathcal{C}\equiv\cosh\theta\sigma_0$, $\mathcal{S}\equiv i\sinh\theta\sigma_y$, and $\theta=\text{atanh}(\Delta/\varepsilon)$. Note that in the case of an asymmetric Josephson junction, one should replace Δ and φ by $\Delta_{1,2}$ and $\varphi_{l,r}$, respectively, according to Fig. 1.

The Usadel equation together with the boundary conditions create a set of coupled complex boundary differential equations. To solve them accurately, we make use of a so-called Riccati parametrization to help in establishing a stable numerical algorithm. Two auxiliary unknown 2×2 matrices, i.e., γ and $\tilde{\gamma}$, are defined for parametrizing the retarded Green's function:

$$G^R(\varepsilon,\mathbf{r})=\begin{pmatrix}(1-\gamma\tilde{\gamma})\Gamma & 2\gamma\tilde{\Gamma}\\ 2\tilde{\gamma}\Gamma & (\tilde{\gamma}\gamma-1)\tilde{\Gamma}\end{pmatrix}, \tag{10}$$

in which $\Gamma=(1+\gamma\tilde{\gamma})^{-1}$ and $\tilde{\Gamma}=(1+\tilde{\gamma}\gamma)^{-1}$. Implementing the Riccati parameterized Green's function, the Usadel equation, Eq. (8), in the nonsuperconducting region of Fig. 1 reads

$$\sum_k\left\{\partial_k^2\gamma-2(\partial_k\gamma)\tilde{\gamma}\Gamma\partial_k\gamma\right\}=-2i\frac{\varepsilon}{D}\gamma, \tag{11a}$$

$$\sum_k\left\{\partial_k^2\tilde{\gamma}-2(\partial_k\tilde{\gamma})\gamma\tilde{\Gamma}\partial_k\tilde{\gamma}\right\}=-2i\frac{\varepsilon}{D}\tilde{\gamma}. \tag{11b}$$

Here we have defined $k\equiv x,y,z$ for the spatial coordinates. To account for ferromagnetism with an arbitrary exchange field, i.e., $\mathbf{h}=(h_x,h_y,h_z)$, one simply needs to add $(\mathbf{h}\cdot\sigma)\gamma-\gamma(\mathbf{h}\cdot\sigma^*)$ and $\tilde{\gamma}(\mathbf{h}\cdot\sigma)-(\mathbf{h}\cdot\sigma^*)\tilde{\gamma}$ into the Usadel equation [Eq. (11a) and (11b), respectively]. Also, the boundary conditions in Eq. (9) for this parametrization scheme at $x=\mp d/2$ are:

$$\partial_x\gamma=\pm\left(2\frac{\mathcal{C}_{1,2}}{\mathcal{S}_{1,2}}+\gamma e^{-i\varphi_{l,r}}-\frac{e^{+i\varphi_{l,r}}}{\gamma}\right)\frac{\mathcal{S}_{1,2}\gamma}{\zeta}, \tag{12a}$$

$$\partial_x\tilde{\gamma}=\pm\left(2\frac{\mathcal{C}_{1,2}}{\mathcal{S}_{1,2}}+\tilde{\gamma}e^{+i\varphi_{l,r}}-\frac{e^{-i\varphi_{l,r}}}{\tilde{\gamma}}\right)\frac{\mathcal{S}_{1,2}\tilde{\gamma}}{\zeta}. \tag{12b}$$

Finally, the charge current density in the equilibrium state is given by

$$\mathbf{J}(\mathbf{r})=\int d\varepsilon\,\text{Tr}\{\rho_z[\hat{G}(\varepsilon,\mathbf{r})\hat{\nabla}\hat{G}(\varepsilon,\mathbf{r})]^K\}, \tag{13}$$

where 'Tr' represents the trace operator. To obtain the total charge current flowing across the junction shown in Fig. 1, one performs an spatial integration over the charge flow component perpendicular to the junction interfaces, namely, $J(x)=\int dy\int dz\,\mathbf{J}_x(\mathbf{r})$. Due to the charge conservation law, $J(x)$ is a constant within the nonsuperconducting region of Fig. 1.

III. RESULTS AND DISCUSSIONS

In the diffusive regime, all lengths are normalized by the superconducting coherence length in the left superconductor, $\xi_S=\sqrt{\hbar D/|\Delta_1|}$, and energies are scaled by the superconducting gap of the left superconducting electrode at zero temperature, $|\Delta_1|$. For the ballistic regime, unless otherwise indicated, all lengths are measured in units of k_F^{-1}, where k_F is the Fermi wave vector in the S regions. We also have the dimensionless zero-temperature coherence length $k_F\xi_0=(2/\pi)(E_{FS}/\Delta_1)$ and fix $k_F\xi_0=100$. As in the diffusive regime, energies are normalized by Δ_1. The measure of mismatch between the Fermi levels is given by the ratio $\Lambda=E_{FM}/E_{FS}$ [34,64,65]. Throughout this paper, we assume $\Delta_2>\Delta_1$, and we consider a uniform magnetization oriented along the z direction so that $\mathbf{h}=h_z=h$. Dimensionless units are implied with $\hbar=k_B=1$.

To gain a detailed view of the supercurrent profile in asymmetric Josephson junctions, we divide the supercurrent into its three constituent parts. According to Fig. 1, these parts consist of (i) the subgap supercurrent J_1, with energies less than Δ_1, (ii) the supergap supercurrent J_2, with energies $\Delta_1<\varepsilon<\Delta_2$, and (iii) the supergap supercurrent J_3, for scattering states with energies larger than Δ_2. When determining the supercurrent via Eq. (6) or Eq. (13), we divide the energy integrals into three parts: $J_1=\int_0^{\Delta_1}\square\,d\varepsilon$, $J_2=\int_{\Delta_1}^{\Delta_2}\square\,d\varepsilon$, and $J_3=\int_{\Delta_2}^{\infty}\square\,d\varepsilon$. For all approaches, the critical supercurrent is calculated in the usual way by finding the maximum of the

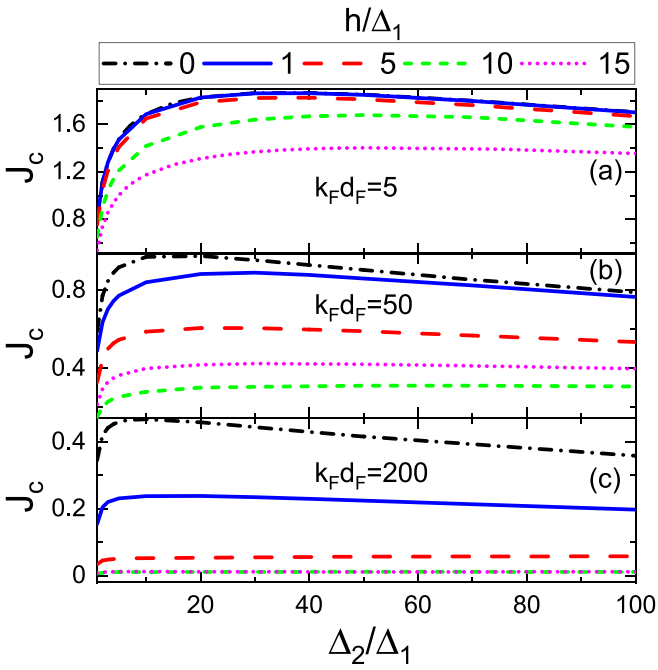

FIG. 2. The critical supercurrent J_c as a function of superconducting gap ratio Δ_2/Δ_1 for three values of the normalized junction thickness: $k_F d_F = 5, 50, 200$, and five values of magnetization strength $h/\Delta_1 = 0, 1, 5, 10, 15$. There is no Fermi level mismatch ($\Lambda = 1$).

supercurrent within a phase difference interval of $\Delta\varphi \in [0, 2\pi]$, namely, $J_c = \max[J(\Delta\varphi)]$.

A. Ballistic S_1NS_2 and S_1FS_2 Josephson junctions

To study the supercurrent profile in ballistic Josephson configurations with asymmetric superconducting gaps, we employ the quantum particle-in-a-box formalism described above [60]. We emphasize that the alternative approach, described in Appendix A, produces similar results and has been used to study various systems, including Rashba-Dresselhaus spin-orbit coupled, type-II Weyl semimetals, and black phosphorus [35,56,57,61,62]. Our comprehensive numerical treatment was also found to agree with certain asymptotic limits, including previous results [58] that considered quasiclassical one-dimensional S_1NS_2 junctions within the short and long junction limits. These limitations were mainly imposed so that analytical solutions could be found. Our fully microscopic approach however does not suffer from these limitations and allows for investigations into asymmetric Josephson configurations with more complicated band structures [35,36,57,60–62]. In what follows, our results cover a broad range of geometrical and material parameters, including junction thickness, Fermi energies, superconducting gap ratio, and magnetization strength. With regards to normalization schemes, the supercurrent density J is normalized by $J_0 \equiv en_e v_F$, where n_e is the bulk electron density and v_F is the Fermi velocity. For clarity, plots involving the supercurrent are also scaled by 10^{-2}.

To begin, we plot the critical supercurrent as a function of Δ_2/Δ_1 in Fig. 2. The strength of the magnetization in the central junction region (see Fig. 1) varies as $h/\Delta_1 = 0, 1, 5, 10, 15$, corresponding to both S_1NS_2 and S_1FS_2 systems. Each panel in Figs. 2(a)–2(c) examines a different junction thickness, with $k_F d_F = 5, 50, 200$, respectively. Considering the nonmagnetic cases first ($h = 0$), it is seen that the correlation between the two superconducting leads (and thus the supercurrent), decays by increasing the junction thickness. This effect becomes more pronounced when considering uniformly magnetized ferromagnets, as the pair-breaking exchange field in the magnet tends to induce damped oscillations in the Cooper pair wave function with a characteristic decay that goes as $1/h$. This causes J_c to become vanishingly small for $k_F d_F = 200$ and $h/\Delta_1 > 5$. Note that the results in Fig. 2 have no Fermi level mismatch ($\Lambda = 1$), which when present can amplify the supercurrent significantly, as will be seen below. One pronounced feature seen in Fig. 2(a) for the short junction limit (i.e., $k_F d_F = 5$) is the enhancement of the critical supercurrent by more than 100% when increasing the gap ratio to $\Delta_2/\Delta_1 \approx 25$, for $h/\Delta_1 \leqslant 5$. This enhancement is diminished as the junction thickness increases whereas the maximum enhancement of the critical current occurs at significantly lower ratios of $\Delta_2/\Delta_1 \approx 1$. Also, as h increases, the critical current maximum gets shifted to larger Δ_2/Δ_1 ratios and becomes relatively insensitive to changes in gap asymmetry beyond $\Delta_2/\Delta_1 \approx 10$.

We next investigate the effects of Fermi level mismatch, characterized by the ratio of the Fermi levels in the two regions: $\Lambda = E_{FM}/E_{FS}$. For F/S junctions, it was previously found [34,64–66] that the characteristic damped oscillations of the singlet pair correlations within the ferromagnet become drastically modified for $\Lambda < 1$. When there is Fermi level mismatch between the junction layers, the energy gap of the system [66] tends to close, as revealed in signatures of the density of states [64–66]. In Fig. 3, we plot total critical supercurrent and its subgap and supergap components against the Fermi energy ratio Λ for a S_1FS_2 junction with $h/\Delta_1 = 15$. Two cases of gap anisotropy are shown in Fig. 3: (b) $\Delta_2/\Delta_1 = 5$ and (c) $\Delta_2/\Delta_1 = 10$. The symmetric case ($\Delta_2/\Delta_1 = 1$) is also shown in panel (a) for comparison purposes. The subgap critical current (J_{c1}) and the supergap (J_{c2}, J_{c3}) critical currents are defined as $J_{ci} \equiv |J_i(\Delta\varphi_c)|$, where $\Delta\varphi_c$ is the phase angle that leads to largest magnitude of the total supercurrent, i.e., $|J(\Delta\varphi_c)| = J_c$. The results reveal that the total critical supercurrent oscillates as a function of Λ. The general profile of J_c remains approximately the same for all gap ratios Δ_2/Δ_1, with an overall amplification of the magnitude of the supercurrent when gap anisotropy is present. For the symmetric case $\Delta_2/\Delta_1 = 1$ in Fig. 3(a), the J_{c2} supergap current component vanishes and J_{c3} is negligibly small. Thus, nearly the entire contribution to the critical supercurrent comes from the J_{c1} subgap component. This is a general feature that arises in short Josephson junctions with symmetric gaps, and it is clear that the Andreev bound states are the dominate mechanism for supercurrent flow. Increasing the superconducting gap ratio to $\Delta_2/\Delta_1 = 5$ [Fig. 3(b)] opens up the transport channel for states between Δ_1 and Δ_2, and thus the J_{c2} supergap current component can contribute considerably to the total supercurrent. Increasing the asymmetry further to $\Delta_2/\Delta_1 = 10$, Fig. 3(c) shows that the J_{c2} contribution becomes even greater. In general, as $\Lambda \to 0$, the number of available states

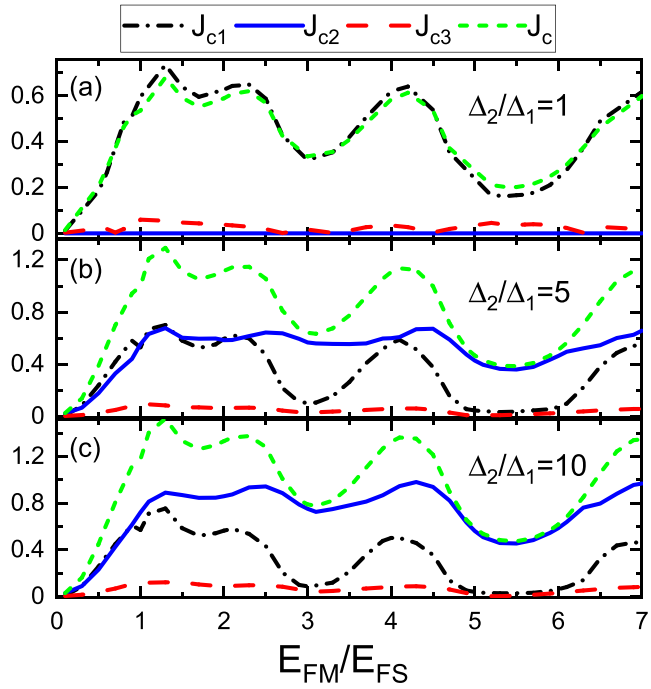

FIG. 3. Total critical supercurrent with its supergap $J_{c2,c3}$ and subgap J_{c1} components as a function of the Fermi level mismatch ratio Λ. The labels show the different parameter values used for the calculations. The junction thickness is set to $k_F d_F = 5$ and the ferromagnetic exchange field is $h/\Delta_1 = 15$.

for supercurrent flow declines to zero. This also is true for the other extreme case of mismatch with $J_c = 0$ as $\Lambda \to \infty$. For the continuum of states with energies exceeding Δ_2, the quasiparticles are no longer confined to the gap regions and lose phase coherence, resulting in J_{c3} being small relative the other supercurrent components.

In Fig. 4, we illustrate how Λ affects the behavior of the subgap (J_{c1}) and the supergap (J_{c2}, J_{c3}) critical current components as functions of Δ_2/Δ_1. Figures 4(a)–4(e) correspond to the nonmagnetic S_1NS_2 case ($h = 0$), while the right set Figs. 4(f)–4(g) exhibits the critical current behavior for S_1FS_2 junctions with $h/\Delta_1 = 15$. Considering first the nonmagnetic case, the left set of panels shows that for a given gap ratio Δ_2/Δ_1, changing Λ modulates the critical current, consistent with the findings shown in Fig. 3. When $\Lambda = 3$, the subgap supercurrent is strongly suppressed and the supergap current dominates the net behavior of the critical current throughout the wide range of Δ_2/Δ_1 considered. Indeed, Andreev bound states with energies less than Δ_1 play little, if any role in the establishment of a supercurrent. For $\Lambda = 2, 4$, the subgap components all have the same trends, including the subgap supercurrent J_{c1}, which exceeds the supergap currents for $\Delta_2/\Delta_1 \lesssim 5$, after which it decays considerably. The supergap current J_{c2} on the other hand, rapidly increases in the region $\Delta_2/\Delta_1 \lesssim 25$, surpassing J_{c1} at $\Delta_2/\Delta_1 \approx 10$, before eventually leveling out close to the total critical current curve. Thus, for $\Delta_2/\Delta_1 \gtrsim 25$, only energies that fall within $\Delta_1 < \epsilon < \Delta_2$ are needed when calculating the critical supercurrent response, while the Andreev bound states with $\epsilon < \Delta_1$ and scattering states with $\epsilon > \Delta_2$ can be neglected. It is evident that there is an intricate and nontrivial relationship between the Fermi level mismatch and the critical current. For situations where there is no mismatch $\Lambda = 1$, Fig. 4(d) shows that the influence of J_{c1} in this regime is significant and cannot be neglected for most gap ratios. In particular, for $\Delta_2/\Delta_1 \leqslant 50$, the J_{c1} component exceeds all other components before slowly decaying at higher values of Δ_2/Δ_1. In Fig. 4(e), where $\Lambda = 0.5$, the crossover point occurs at the much smaller $\Delta_2/\Delta_1 \approx 6$, indicating that both J_{c1} and J_{c2} must be accounted for, even for moderate Δ_2/Δ_1 ratios. These results indicate that when characterizing the supercurrent decomposition, the degree of Fermi level mismatch and gap mismatch play an important role in which quasiparticle energies contribute to the supercurrent response. Also, a notable feature in Figs. 4(a) and 4(b) is that J_{c2} sometimes exceeds the total supercurrent. This arises mainly due to the subgap J_1 and supergap J_2 currents flowing in opposite directions. This important point shall be discussed further below.

Next, when the central layer possesses a uniform magnetization, the adjacent panels in Figs. 4(f)–4(j) reveal a clear modification to all three components of the critical current. For each of the four cases of Fermi level mismatch, the component J_{c1} has an extremely slow decay for gap ratios within $\Delta_2/\Delta_1 \gtrsim 5$. Thus within this regime, and for quasiparticle energies with $\epsilon > 5\Delta_1$, the critical current is insensitive to the relative gap ratios characterizing the superconducting leads. When $\Delta_2/\Delta_1 = 1$, corresponding to the commonly used scenario of no asymmetry in the gaps, the supergap component J_{c2} vanishes. In Figs. 4(f) and 4(h), when $\Lambda = 4$ and $\Lambda = 2$, respectively, the subgap component J_{c1} dominates all other critical current components for relatively small gap ratios $\Delta_2/\Delta_1 \lesssim 2$. Both of the two components J_{c1} and J_{c2} contribute equally to the critical current for $\Delta_2/\Delta_1 \approx 5$, with J_{c2} the largest contributor for larger gap asymmetry. The picture changes considerably when $\Lambda = 3$, as Fig. 4(g) illustrates that the conventional Andreev bound states characterized by J_{c1} play a minor role in the net supercurrent behavior when $\Delta_2/\Delta_1 \gtrsim 2$. When the Fermi levels are the same in each segment of the junction [Fig. 4(i)], the subgap component becomes more influential with J_{c1} and J_{c2} crossing at $\Delta_2/\Delta_1 \approx 4.5$. Finally, in Fig. 4(j), we consider $E_{FM} < E_F$ and $\Lambda = 0.5$. In this regime, both the subgap and supergap components contribute nearly equally for most gap ratios $\Delta_2/\Delta_1 \gtrsim 15$, while less asymmetry again has J_{c1} the larger of the components. It should be noted that the enhancement of each of the current components against Δ_2/Δ_1 occurs within a smaller interval compared to the S_1NS_2 junction.

In conventional S_1FS_2 junctions, the exchange field induces damped oscillations in the pair potential and the Josephson current exhibits oscillations as a function of the ferromagnet exchange field [67]. To see how this picture may change for asymmetric junctions, we present in Fig. 5 the behavior of the critical supercurrent and its components versus the normalized exchange field h/Δ_1. The study covers the full range from nonmagnetic, $h/\Delta_1 = 0$, to half-metallic, $h/\Delta_1 \approx 160$, where only one spin band is available. Each panel corresponds to one of the five different Fermi level mismatch ratios Λ that are considered (as labeled). To further clarify the importance of supergap and subgap supercurrents when there is gap asymmetry, we have considered $\Delta_2/\Delta_1 = 1$

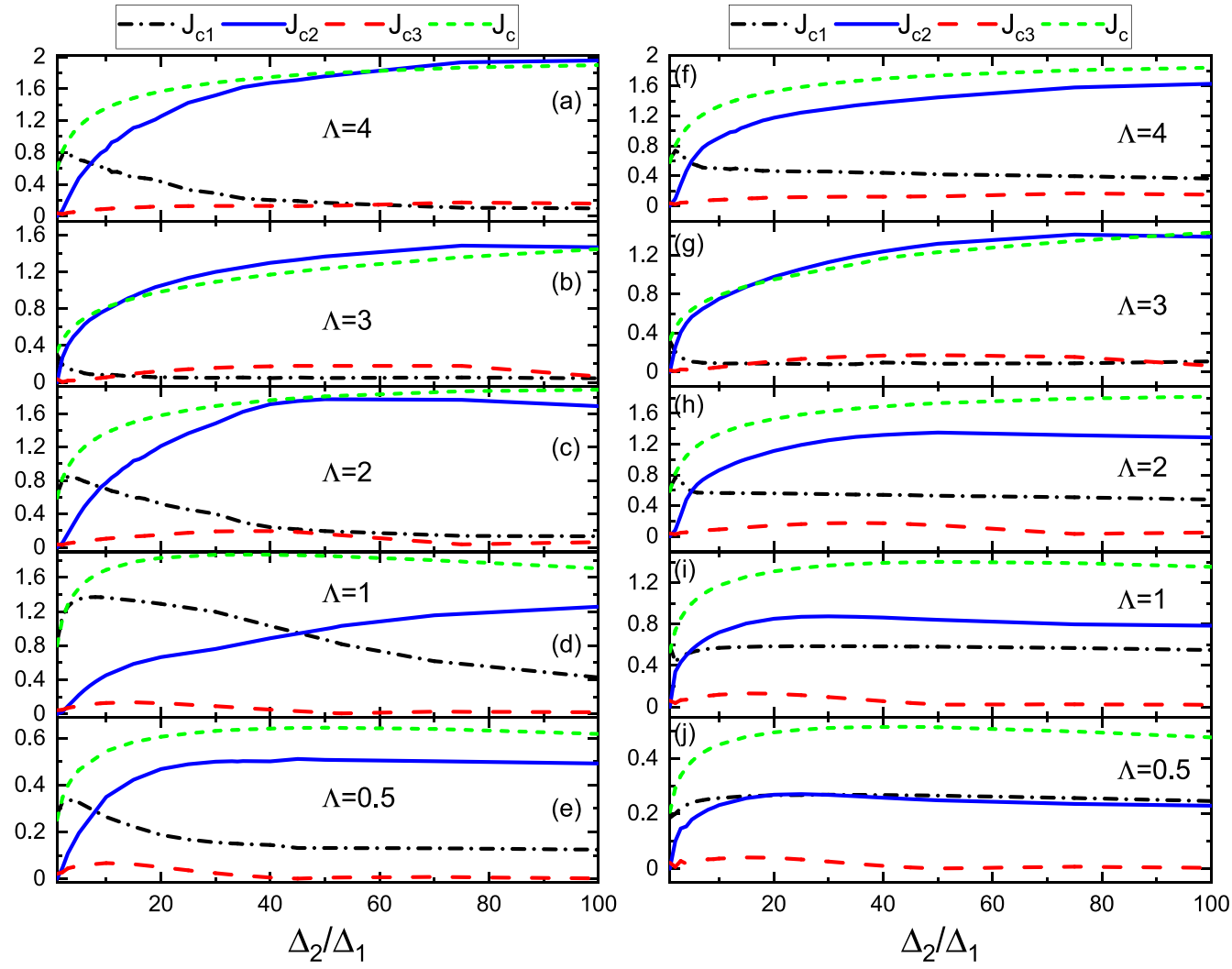

FIG. 4. Critical supercurrent J_c with its subgap J_{c1} and supergap J_{c2}, J_{c3} components shown as functions of the superconducting gap ratio Δ_2/Δ_1. The junction thickness is set at $k_F d_F = 5$ for various values of $\Lambda = E_{FM}/E_F = 0.5, 1, 2, 3, 4$. The magnetization is set to zero in (a)–(e) while $h/\Delta_1 = 15$ in panels (f)–(j).

in Figs. 5(a)–5(e) and set $\Delta_2/\Delta_1 = 5$ in Figs. 5(f)–5(j). The results in Figs. 5(a)–5(e) show that for symmetric junctions ($\Delta_2/\Delta_1 = 1$), the subgap supercurrent J_{c1} is the dominant current component over the entire range of magnetization strengths and Fermi level mismatches. The supergap contribution J_{c2} to the total critical current of course vanishes entirely, while the J_{c3} component arising from states in the continuum is negligible. Hence, when the gap asymmetry vanishes ($\Delta_2/\Delta_1 = 1$), the behavior of the total supercurrent can be well captured through J_{c1} only. It then suffices to take only the subgap current components to accurately account for the general features of the supercurrent, including its reversal in certain regions where it displays cusps for a given Λ and h/Δ_1 [see, e.g., $h/\Delta_1 \approx 30, 110$ in Fig. 5(d)]. Examining Figs. 5(a)–5(e), it is clear that the critical current is nonmonotonic with a modulation that strongly depends on Λ. Interestingly, tuning the Fermi level mismatch to $\Lambda = 3$ creates a situation where increasing the exchange field beyond the first cusp at $h/\Delta_1 \approx 90$ results in a dramatic rise in the supercurrent response. Indeed, Fig. 5(b) demonstrates that compared to a nonmagnetic junction ($h = 0$), using a half-metallic insert ($h/\Delta_1 \approx 160$) causes J_c to nearly double.

If gap asymmetry is now introduced into the system ($\Delta_2/\Delta_1 = 5$), Figs. 5(f)–5(j) show the emergence of the J_{c2} component, which can at times make sizable contributions to the total supercurrent. It is evident that the cusps in J_c where the current reverses can be ascribed to the cumulative effects of J_{c1} and J_{c2}, regardless of the Fermi level ratio Λ. Therefore, when $\Delta_2/\Delta_1 \neq 1$, the subgap current component alone is unable to provide an accurate and complete picture of the total supercurrent. Further details on the origins of both the subgap and supergap supercurrent components in terms of their discrete energy spectra and energy-resolved supercurrents is given in Appendix B.

The study of the critical current dependence on the ferromagnet thickness in S_1FS_2 Josephson junctions has been extensively investigated both theoretically [67] and experimentally [6,11]. Proximity effects arising from the coupling of the outer superconducting banks and ferromagnet leads to oscillations of the pair amplitude in the ferromagnet. Under certain conditions, these oscillations can cause the ground

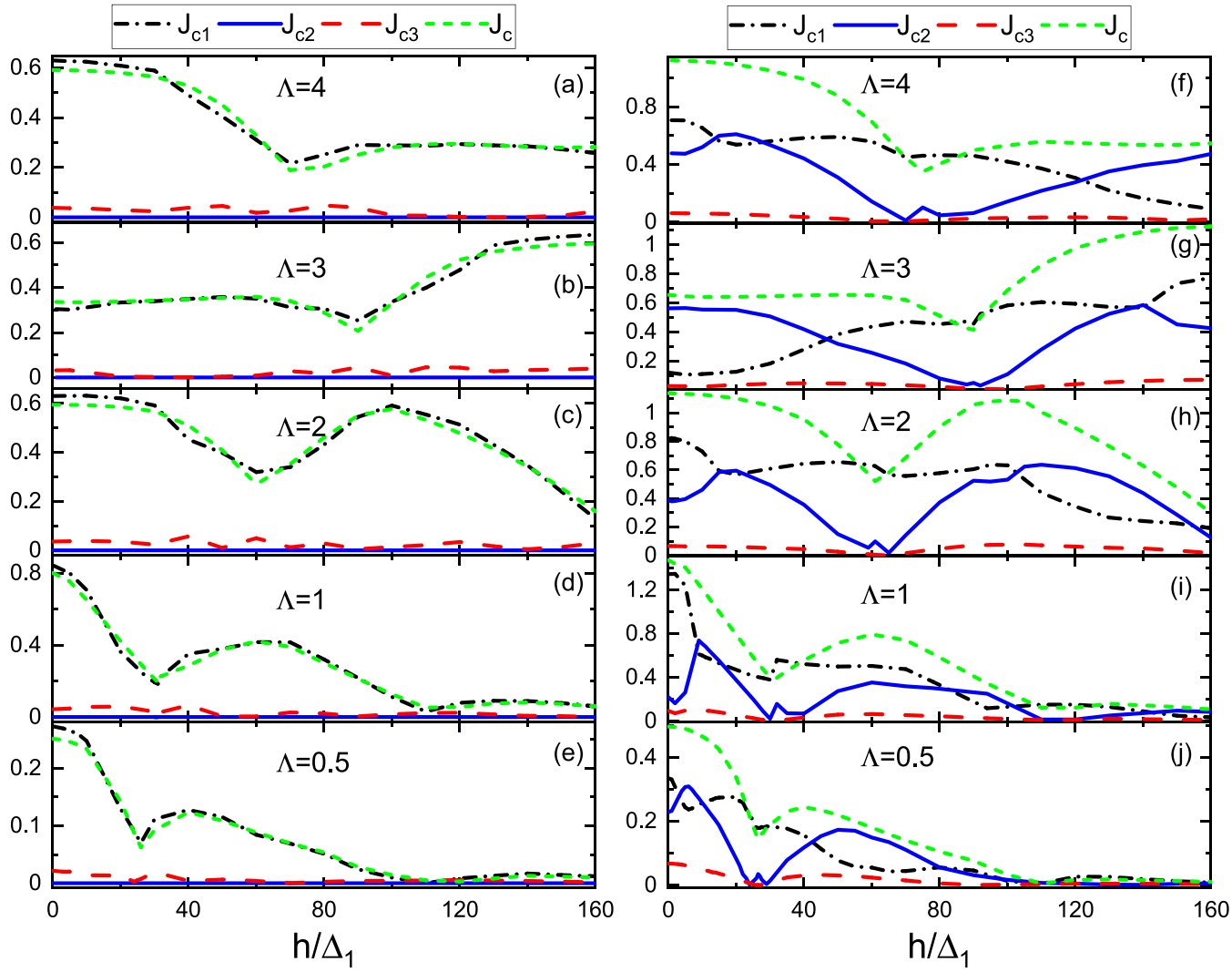

FIG. 5. Critical supercurrent with its supergap and subgap components as a function of uniform magnetization strength h/Δ_1. In the left column [panels (a)–(e)] the superconducting gap ratio is set to $\Delta_2/\Delta_1 = 1$ while in the right column [panels (f)–(j)] $\Delta_2/\Delta_1 = 5$.

state of the system to transition to a state with $\Delta\varphi = \pi$. During these transitions, the supercurrent reverses direction and reveals itself as cusps near the minima of the critical current. Unfortunately, the study of transport in clean ferromagnetic Josephson junctions with Fermi level mismatch and gap asymmetry from a purely microscopic perspective is lacking. Therefore, to address these deficiencies, we present in Fig. 6 the critical current and its associated components as a function of normalized junction thickness $k_F d_F$. The junction possesses a gap asymmetry of $\Delta_2/\Delta_1 = 5$, and two different values of the Fermi level mismatch parameter $\Lambda = 1, 2$ are considered. Since the damped oscillations in the ferromagnet are governed by the spin-split Fermi wave vectors there, having E_F vary across different segments of the Josephson junction can modify the oscillatory period of the pair amplitude. The spin splitting in the ferromagnet introduces the length scale ξ_F set by the difference in the spin up and spin down Fermi wave vectors, $\xi_F \propto (k_{F\uparrow} - k_{F\downarrow})^{-1}$. Accordingly, the cusps are found to repeat in intervals of $\pi\xi_F \approx \pi E_F\sqrt{\Lambda}/h$, which for $h/\Delta_1 = 15$ and $\Lambda = 1, 2$ corresponds to $\pi\xi_F \approx 32.9, 46.9$, respectively. This is seen when comparing Figs. 6(a) and 6(b). Note that the damped oscillations in the critical current with thickness have also been observed in the critical temperature for ballistic spin valves [45].

As seen in Fig. 6, for a given Λ, the supergap component J_{c2} contributes the most for small ferromagnet thicknesses. To explore this further, Fig. 7 displays the critical current and its components over a narrower range of thicknesses for the S_1FS_2 configuration. To reveal how the oscillations and magnitude of the supercurrent changes with variations in the Fermi level ratios, a broad range of mismatch parameters Λ is considered. As seen in Figs. 7(a)–7(e), the J_{c3} component is negligible, as scattering states again contribute little to the supercurrent response. The total supercurrent oscillates as a function of $k_F d_F$, but in contrast to Fig. 6, the oscillations over the much smaller Fermi length scale are now discernible. These small-scale oscillations are neglected in quasiclassical treatments where atomic scale features are eliminated. Moreover, increasing Λ decreases the period of oscillations in Figs. 3(a)–3(e), which is consistent with the corresponding increases in the ratios of the Fermi wave vectors in the ferromagnet and superconductor regions k_{FM}/k_F. For Fermi

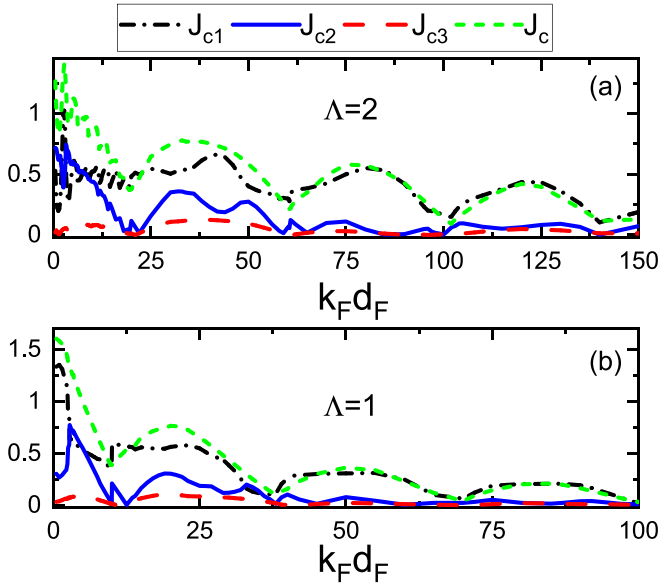

FIG. 6. Critical supercurrent with its subgap and supergap components as a function of the normalized junction thickness $k_F d_F$ for an asymmetric S_1FS_2 junction. The gap asymmetry for both panels (a) and (b) corresponds to $\Delta_2/\Delta_1 = 5$ and the normalized exchange field is set to $h/\Delta_1 = 15$. In (a) the Fermi level mismatch is set to $\Lambda = 2$, while in (b) the relative Fermi levels are the same ($\Lambda = 1$).

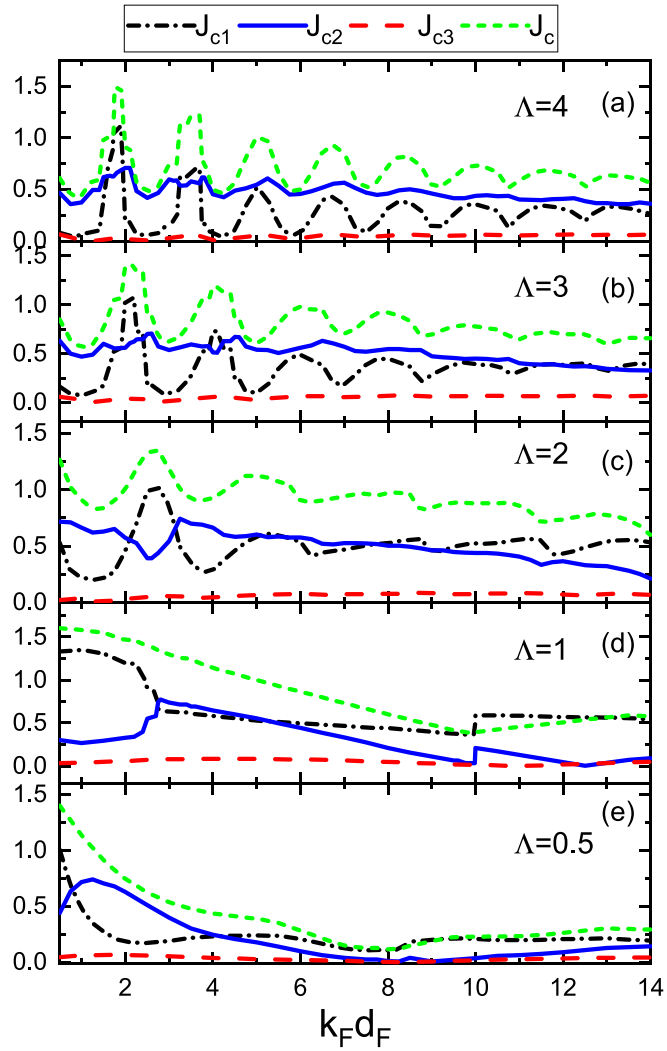

FIG. 7. Critical supercurrent with its subgap and supergap components as a function of junction thickness for differing chemical potential ratios $\Lambda = 0.5, 1, 2, 3, 4$. The superconducting gap ratio and exchange field strength are set to $\Delta_2/\Delta_1 = 5$ and $h/\Delta_1 = 15$, respectively.

level ratios corresponding to $\Lambda = 4$ and $\Lambda = 3$, Figs. 3(a) and 3(b) illustrate that while J_{c2} has gradual variations as the thickness changes, the subgap component J_{c1} has pronounced oscillations that periodically vanish (or nearly so) for thin ferromagnets. Therefore certain thicknesses can be chosen that result in maximal supercurrent flow that is almost entirely comprised of supergap J_{c2} states. As the difference between Fermi levels lessens, Figs. 3(c) and 3(d) show that the oscillatory behavior dampens out for thicker ferromagnets. Finally in Fig. 3(e), we find that the critical current mainly declines rapidly as the normalized thickness increases and then levels off to greatly diminished values.

We now present the current-phase-relations for the total supercurrent and its components at specific parameter values corresponding to points of interest found in earlier critical supercurrent plots. In Figs. 8(a)–8(d), we have set the exchange field h to zero and consider a S_1NS_2 configuration with varying degrees of gap asymmetry. As seen in Fig. 8(a), when there is no gap asymmetry ($\Delta_2/\Delta_1 = 1$), the J_3 component is slightly discernible, as states in the continuum contribute little to the supercurrent in short junctions. Also, the J_2 supergap component vanishes, as expected for the symmetric case. Thus the current in this case is carried nearly entirely by bound states. Examining Figs. 8(b)–8(d), it is evident that by increasing the asymmetry through the superconducting gap ratio, Δ_2/Δ_1, a supergap current J_2 emerges and begins to play a more impactful role in the total supercurrent response. In contrast, the subgap current J_1 accordingly becomes weaker, as its contribution to at least 50% of the total supercurrent is limited to relatively narrow phase differences, $130^\circ \lesssim \Delta\varphi \lesssim 160^\circ$. Despite the significant changes to J_1 and J_2, the overall supercurrent, J_{tot}, increases but retains its overall profile. Increasing Δ_2/Δ_1 also is seen to enhance the supercurrent overall, while shifting the supercurrent peaks to smaller $\Delta\varphi$. The enhancement of the supercurrent follows in part from the broadening of the discrete energy states that occurs for larger ratios Δ_2/Δ_1 [see Appendix B]. The microscopic numerical results presented in Figs. 8(a)–8(d) are also consistent with one-dimensional quasiclassical models [58]. In Appendix B, Fig. 12 reveals the interplay between the bound and scattering states related to Fig. 8 and are discussed in terms of the energy-resolved and phase-resolved current density.

Next, upon incorporating a uniform magnetization of $h/\Delta_1 = 15$, Figs. 8(e)–8(h) illustrate how this leads to a drastic modification to the profiles of the current-phase relations. For S_1FS_2 junctions, we find a slight drop to the overall net supercurrent response for the whole range of gap asymmetries considered. Increasing the gap asymmetry tends to enhance the overall supercurrent, but the general current-phase profile remains relatively unchanged, with minimal change in the

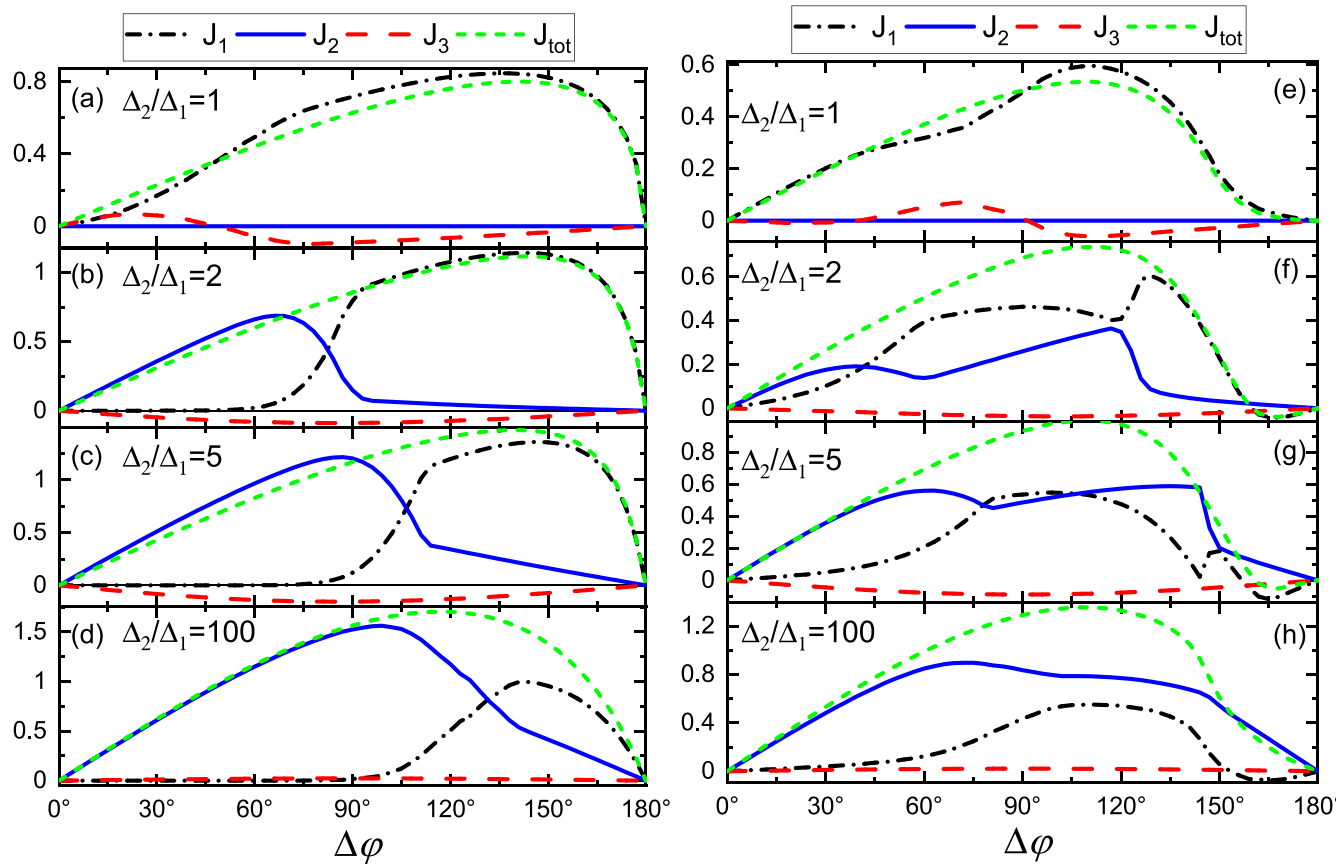

FIG. 8. Supergap ($J_{2,3}$) and subgap (J_1) current components as a function of the superconducting phase difference $\Delta\varphi$. (a)–(d) The supercurrent profile for a S_1NS_2 junction. (e)–(h) The supercurrent profile for a S_1FS_2 junction with $h/\Delta_1 = 15$. The junction thickness is set fixed to $k_F d_F = 5$, and the relative Fermi levels are equal ($\Lambda = 1$).

peak locations. One noticeable difference however occurs for $\Delta_2/\Delta_1 = 2, 5$, where the supercurrent undergoes a current reversal at $\varphi \approx 162^\circ$. We find that similar to the symmetric S_1NS_2 junction, Fig. 8(e) shows a small contribution from J_3 arising from scattering states ($\epsilon > \Delta_1$) when there is gap symmetry. For extreme gap asymmetry $\Delta_2/\Delta_1 = 100$, shown in Fig. 8(h), the supergap component J_2 is the main contributor to the overall current, and we see that although J_1 has broadened compared to the nonmagnetic case, it never exceeds approximately 40% of the total critical current.

To elaborate on the damped oscillations in the pairing correlations that induce 0-π transitions responsible for supercurrent reversals and cusps in the critical current profile of asymmetric junctions, we have studied the exchange field dependence of the current-phase relations in Fig. 9. The total supercurrent $J_{\rm tot}$ is shown alongside its constitutive components $J_{1,2,3}$. As a representative parameter set, we have chosen the first crossover state in Fig. 5(i), which occurs around $h/\Delta_1 \approx 32$. Therefore, in Figs. 9(a)–9(e) we set $\Delta_2/\Delta_1 = 5$, $\Lambda = 1$, and $k_F d_F = 5$ and vary the normalized magnetization according to $h/\Delta_1 = 26, 28, 31, 34, 36$, respectively. As seen, the overall profile and magnitude of the subgap supercurrent component J_1 is relatively unaffected as the exchange field increases. The supergap current J_2 however experiences a transition in which it goes from entirely positive for $h/\Delta_1 = 26$ to negative for most phase differences $\Delta\varphi$ when $h/\Delta_1 = 36$. This results in an overall suppression of the total supercurrent, illustrating the influential control of the J_2 component on the total supercurrent. Therefore, adjacent to a 0-π crossover, the supergap J_2 and subgap J_1 current components propagate in opposite directions, creating a competing situation. Below, we shall see that a similar occurrence takes place near the 0-π transition point in the diffusive regime. It should be noted that the supercurrent in the ballistic regime involves the superposition of quasiparticle trajectories undergoing normal and Andreev reflections at the two superconductor interfaces. Due to the microscopic method used, length scales as small as the Fermi wavelength are included, permitting the capture of Friedel-like oscillations [68], which emerge as highly oscillatory signatures in the supercurrent response for small normalized layer thicknesses $k_F d_F$. The resonant modes are also highly sensitive to the relevant geometrical and material parameters such as the junction length, Fermi level, magnetization strength, and superconducting gap ratio, all of which intricately combine to give the observed small oscillations in, e.g., Figs. 7 and 8. Nonetheless, the final conclusions and central findings are clearly independent of these subfeatures.

B. Diffusive S_1NS_2 and S_1FS_2 Josephson junctions

We now consider the supercurrent response in asymmetric diffusive Josephson junctions. To properly capture quasiparticles with energies deemed relevant to the net supercurrent, we have set an energy cutoff of $\varepsilon_{\rm max} = 25\Delta_1$ when performing

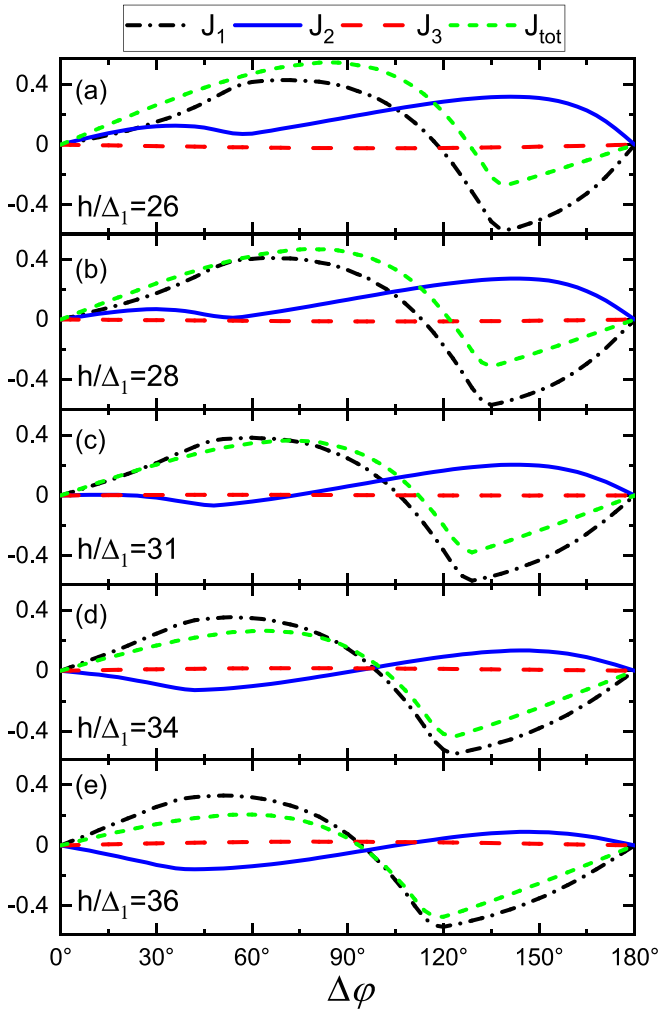

FIG. 9. Total current-phase relation with its supergap and subgap components for several key exchange-field values around a current reversal point. The superconducting gap ratio is set to $\Delta_2/\Delta_1 = 5$, the junction thickness is $k_F d_F = 5$, and there is no mismatch in Fermi levels ($\Lambda = 1$).

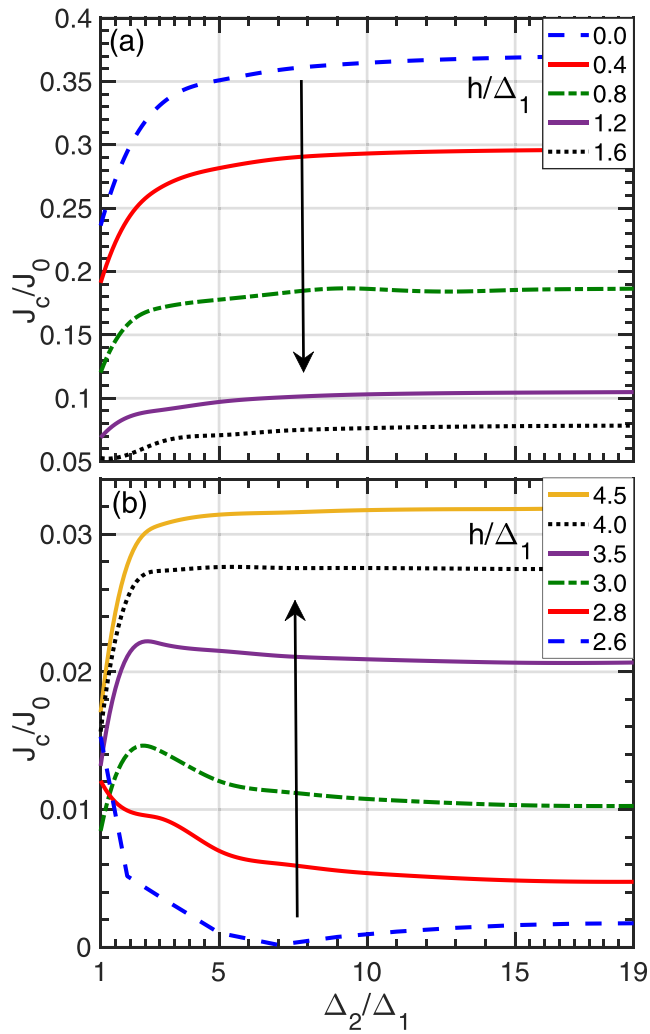

FIG. 10. Critical supercurrent in a diffusive S_1FS_2 Josephson junction as a function of Δ_2/Δ_1. The junction thickness is fixed at $d = 0.8\xi_S$ and various values of the normalized exchange field are considered: $h/\Delta_1 = 0, 0.4, 0.8, 1.2, 1.6, 2.6, 2.8, 3.0, 3.5, 4.0, 4.5$.

the integration over quasiparticle energies. We have also used representative values for the junction thickness and interface opacity, with $d = 0.8\xi_S$ and $\zeta = 4$, respectively. The maximum supercurrent flow as a function of Δ_2/Δ_1 is shown in Fig. 10. The maximum of critical supercurrent occurs when the magnetization in the junction vanishes. As seen, the critical supercurrent enhances by 50% when $\Delta_2/\Delta_1 \approx 10$ and $h = 0$. Upon increasing the strength of the uniform exchange field h, the critical supercurrent becomes suppressed. For weak ferromagnets with exchange energies corresponding to $h \sim 2.6\Delta_1$, the supercurrent undergoes a sign reversal as the gap asymmetry Δ_2/Δ_1 is varied. By further increasing h/Δ_1 to 2.8, 3.0, 4.0, 4.5, the overall critical supercurrent is enhanced and returns to its previous monotonic growth as a function of Δ_2/Δ_1. In contrast to the other normalized exchange field strengths, the case with $h/\Delta_1 = 2.6$ exhibits a clear supercurrent suppression for $\Delta_2/\Delta_1 \lesssim 7$. Increasing the exchange field to $h/\Delta_1 = 2.8, 3.0$ causes the supercurrent to have a short-lived enhancement, and a subsequent cusp at $\Delta_2/\Delta_1 \approx 3$, before slowly declining as the gap ratio increases. To create a stable numerical scheme, we have introduced a small imaginary part $\delta = 0.005$ to the energy of the quasiparticles ε. This imaginary part can act as a source of inelastic scattering, which if increased, can wash out the dominant and important parts of the curves, such as the overall supercurrent response and associated 0-π transitions. For a relatively small imaginary part, as is considered throughout our numerical study, the algorithm can at times introduce insignificant artifacts that show up as small oscillations in the supercurrent.

To gain a comprehensive picture of the supercurrent in a diffusive asymmetric Josephson junction, we have plotted the components $J_{1,2,3}(\Delta\varphi)$ and total supercurrent $J(\Delta\varphi)$ in Fig. 11. Various levels of gap asymmetry are shown corresponding to $\Delta_2/\Delta_1 = 1.0, 1.5, 2.0, 2.6$. The nonmagnetic S_1NS_2 case is shown in Figs. 11(a)–11(d), whereas Figs. 11(e)–11(h) correspond to a S_1FS_2 junction. As seen

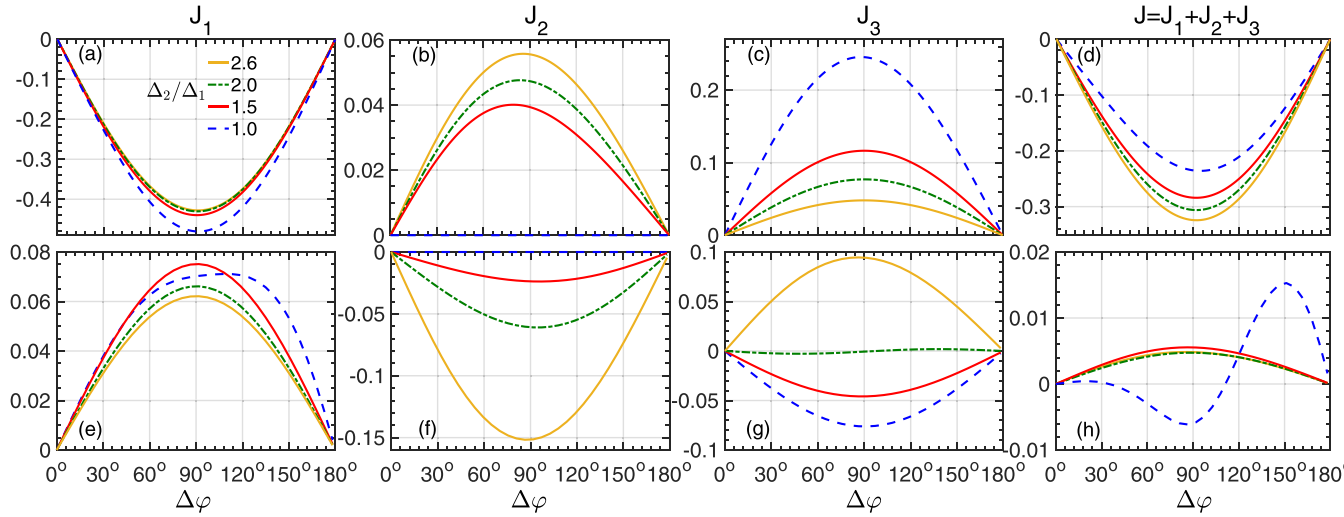

FIG. 11. The three components of supercurrent at four different values of the gap anisotropy ratio: $\Delta_2/\Delta_1 = 1.0$, 1.5, 2.0, and 2.6. In (a)–(d), the exchange field h is set to zero, and in (e)–(h), we set to $h = 2.6\Delta_1$.

for both cases, when $\Delta_2 = \Delta_1$, the $J_2(\Delta\varphi)$ component vanishes, as expected. Also, there is an overall reduction of the supercurrent magnitudes in the magnetic case. Other than their magnitudes, the current-phase relations of the $J_2(\Delta\varphi)$ components are similar for S_1NS_2 and S_1FS_2 junctions with asymmetric superconducting gaps (albeit with different signs). The subgap supercurrent $J_1(\Delta\varphi)$ behaves slightly differently for S_1NS_2 and S_1FS_2 junctions. In the latter case, when $\Delta_2 = \Delta_1$, the supercurrent deviates strongly from the usual sinusoidal relation. In contrast to the S_1NS_2 case, the component $J_3(\Delta\varphi)$ shows a $\sim \sin 2\Delta\varphi$ relation around $\Delta_2 \approx 2\Delta_1$ and changes sign for larger values. The competition between these components results in the total supercurrents shown in the far right panels. As is apparent, unlike the strikingly different responses of $J_{1,2,3}(\Delta\varphi)$ for $\Delta_2 > \Delta_1$, the total supercurrent changes uniformly except when transitioning from $\Delta_2 = \Delta_1$ to $\Delta_2 > \Delta_1$ for the S_1FS_2 junction with $h = 2.6\Delta_1$. This variation results in the form of the current-phase relation changing from $\sim \sin 2\Delta\varphi$ to $\sim \sin \Delta\varphi$. Note that the total supercurrent response in Fig. 11(h) has the form $\sim \sin 2\Delta\varphi$, which appears due to the competition between the subgap supercurrent states comprising $J_1(\Delta\varphi)$ and the scattering states which embody $J_3(\Delta\varphi) \sim \sin \Delta\varphi$. The competition originates from the opposite propagation directions of the $J_1(\Delta\varphi)$ and $J_3(\Delta\varphi)$ current components. These findings thus complement the ballistic results that found many instances where supergap modes must be accounted for appropriately to obtain accurate and reliable results. Further insight into the supergap and subgap responses are presented in Appendix C, where the energy-resolved and phase-resolved supercurrent density is analyzed.

IV. CONCLUSIONS

By employing complementary numerical approaches in the ballistic and diffusive regimes, we have performed a comprehensive study of supercurrent flow through asymmetric S_1NS_2 and S_1FS_2 Josephson junctions where the superconducting gap in the $S_{1,2}$ regions are unequal, i.e., $\Delta_2 \neq \Delta_1$. In the ballistic regime, we have directly solved the Bogoliubov de-Gennes Hamiltonian that allows for exploring a parameter space with a wide range of energy and length scales, whereas when impurities and disorder are present, we make use of the full proximity limit of the quasiclassical regime. Our results found that for asymmetric junctions with $\Delta_2/\Delta_1 \approx 25, 10$, the critical supercurrent can be enhanced by more than 100% and 50% in the ballistic and diffusive S_1NS_2 cases, respectively. Our results in the ballistic cases reveal that when $\Delta_2/\Delta_1 = 1$, the subgap current is the main contributor to total supercurrent. Introducing an imbalance to the superconducting gap ratio $\Delta_2/\Delta_1 > 1$, the supergap currents were discovered to play key roles and for certain parameter values were the main contributors to the total supercurrent. Through our investigations of asymmetric junctions (with $\Delta_2/\Delta_1 > 1$), the current phase relations with their supergap and subgap current components were explored around 0-π current crossover points. We found that the emergence of second harmonics in the current-phase relations of S_1FS_2 junctions is a direct consequence of the competition between subgap and supergap current components with opposite flow directions. It was shown in an earlier work [58] that supergap currents are relatively insensitive to temperature compared to the subgap component, as the former originates from evanescent modes in the continuum, whereas the latter is carried through resonant bound states. Therefore, the findings of this paper should serve to stimulate experiments that pave the way for designing new superconducting devices that utilize robust supergap currents. The asymmetric S_1NS_2 and S_1FS_2 structures studied here can apply to Josephson configurations where the amplitude of the superconducting gaps might fluctuate independently when the system is subject to a strong external magnetic field or high temperatures near the critical temperature. Furthermore, the enhancement of the critical supercurrent due to $\Delta_1 \neq \Delta_2$ can be beneficial in magnetic Josephson junctions that suffer from weakened currents in the presence of ferromagnetism.

ACKNOWLEDGMENTS

K.H. is supported in part by ONR and a grant of HPC resources from the DOD HPCMP.

APPENDIX A: ALTERNATIVE WAVE-FUNCTION APPROACH: BALLISTIC REGIME

The method outlined in Sec. II A provides an effective way to solve Josephson junction systems with limited approximations in the ballistic regime. There also exists wave-function approaches that can provide exact solutions, one of which we outline below [35,56,57,61,62].

To simulate the low-energy physics of heterostructures in the presence of a magnetization with arbitrary direction, $\mathbf{h} = (h_x, h_y, h_z)$, one employs an effective single-particle Hamiltonian:

$$H = \frac{1}{2}\int d\mathbf{p}\,\hat{\psi}^\dagger(\mathbf{p})\left[\frac{\mathbf{p}^2}{2m} + \boldsymbol{\sigma}\cdot\mathbf{h}\right]\hat{\psi}(\mathbf{p}), \tag{A1}$$

where $\mathbf{p} = (p_x, p_y, p_z)$ is the momentum and m is the effective mass of a charged particle. The associated field operator in spin space is given by $\hat{\psi} = (\psi_\uparrow, \psi_\downarrow)^{\mathrm{T}}$ and $\boldsymbol{\sigma} = (\sigma_x, \sigma_y, \sigma_z)$ is a vector comprised of Pauli matrices. The spin-singlet superconductivity in the BCS scenario can be described by the following electron-electron amplitudes:

$$\Delta\langle\psi_\uparrow^\dagger\psi_\downarrow^\dagger\rangle + \mathrm{H.c.} \tag{A2}$$

Accounting for the electron-electron amplitudes in the BdG formalism, the low-energy Hamiltonian in spin-Nambu space reads:

$$\mathcal{H}(\mathbf{p}) = \begin{pmatrix} H(\mathbf{p}) - \mu\hat{1} & \hat{\Delta} \\ \hat{\Delta}^\dagger & -H^\dagger(-\mathbf{p}) + \mu\hat{1} \end{pmatrix}, \tag{A3}$$

in which $\hat{\Delta}$ is the superconducting gap $\hat{\Delta} \equiv (\Delta, -\Delta)e^{i\varphi_{l,r}}$, and μ is the chemical potential. The field operators in the rotated spin-Nambu space are given by $\hat{\psi} = (\psi_\uparrow, \psi_\downarrow, \psi_\downarrow^\dagger, -\psi_\uparrow^\dagger)^{\mathrm{T}}$. The continuity equation for charged carriers is written:

$$\frac{\partial\rho_{\mathrm{c}}}{\partial t} = \lim_{\mathbf{r}\to\mathbf{r}'}\sum_{\sigma\tau\sigma'\tau'}\frac{1}{i}\big[\psi_{\sigma\tau}^\dagger(\mathbf{r}')\mathcal{H}_{\sigma\tau\sigma'\tau'}(\mathbf{r})\psi_{\sigma'\tau'}(\mathbf{r}) - \psi_{\sigma\tau}^\dagger(\mathbf{r}')\mathcal{H}_{\sigma\tau\sigma'\tau'}^\dagger(\mathbf{r}')\psi_{\sigma'\tau'}(\mathbf{r})\big], \tag{A4}$$

where $\mathcal{H}_{\sigma\tau\sigma'\tau'}$ is the component form of Eq. (A3) and σ, τ indices label the spin and particle-hole degrees of freedom, respectively. In a situation where no sink or source of charge is present, the time variation of charge density vanishes: $\partial_t\rho_{\mathrm{c}} \equiv 0$. Accounting for the current conservation law, the charge current density can be expressed by:

$$\mathbf{J} = \int d\mathbf{r}\{\hat{\psi}^\dagger(\mathbf{r})\overrightarrow{\mathcal{H}}(\mathbf{r})\hat{\psi}(\mathbf{r}) - \hat{\psi}^\dagger(\mathbf{r})\overleftarrow{\mathcal{H}}(\mathbf{r})\hat{\psi}(\mathbf{r})\}, \tag{A5}$$

where the real-space Hamiltonian $\mathcal{H}(\mathbf{r})$ is obtained by substituting $\mathbf{p} \equiv -im^{-1}(\partial_x, \partial_y, \partial_z)$ in Eq. (A3). The arrows indicate the specific wave functions that the Hamiltonian operates on. To obtain the supercurrent, one computes the current density perpendicular to the interfaces, in our geometry shown in Fig. 1, J_x, and integrates over the junction cross section in the y and z directions: $J(\Delta\varphi) = J_0\iint dzdy\mathbf{J}_x(x, y, z, \Delta\varphi)$. Here $J_0 = 2e|\Delta|$, and e is the electron charge. Upon diagonalizing $\mathcal{H}(\mathbf{p})$ in Eq. (A3), one obtains the electronic wave functions $\hat{\psi}_{l,m,r}(\mathbf{p})$ within the left (l), middle (m), and right (r) regions. Next, the wave functions are matched at the left $\hat{\psi}_l = \hat{\psi}_m|_{x=0}$ and the right boundaries $\hat{\psi}_m = \hat{\psi}_r|_{x=d}$. The continuity conditions must also be satisfied: $(\partial_{\mathbf{p}}\mathcal{H}_l)_{\mathbf{r}}\hat{\psi}_l = (\partial_{\mathbf{p}}\mathcal{H}_m)_{\mathbf{r}}\hat{\psi}_m|_{x=0}$, $(\partial_{\mathbf{p}}\mathcal{H}_m)_{\mathbf{r}}\hat{\psi}_m = (\partial_{\mathbf{p}}\mathcal{H}_r)_{\mathbf{r}}\hat{\psi}_r|_{x=d}$. The index $\mathbf{r}$ indicates a switch to real space after taking the derivatives in momentum space. It is important to note that we apply no simplifying assumptions and approximations to the wave functions in the numerical calculations. This however results in highly complicated and lengthy expressions for the wave functions and supercurrent. We therefore are only able to evaluate them numerically.

APPENDIX B: ENERGY DISPERSION AND ENERGY-RESOLVED SUPERCURRENT DENSITY: BALLISTIC REGIME

When calculating the supercurrent via Eq. (6), all positive energy states within an energy cutoff ϵ_c are summed over, with ϵ_c chosen sufficiently large so that including any additional states has no distinguishable effects on the results. It is important to note that when summing the quantum states for the supercurrent, the summation implicitly includes an integration over the continuum of states with transverse energy

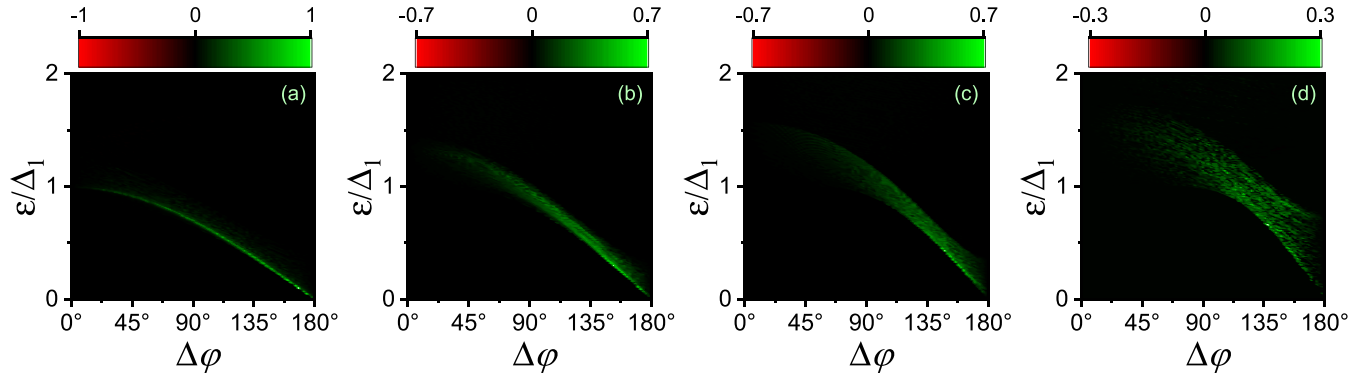

FIG. 12. Total supercurrent density mappings as a function of phase difference $\Delta\varphi$ and energy ε for a S_1NS_2 Josephson junction with varying levels of gap asymmetry: (a) $\Delta_2/\Delta_1 = 1$, (b) $\Delta_2/\Delta_1 = 2$, (c) $\Delta_2/\Delta_1 = 5$, and (d) $\Delta_2/\Delta_1 = 100$. The Fermi levels are equal throughout the system ($\Lambda = 1$).

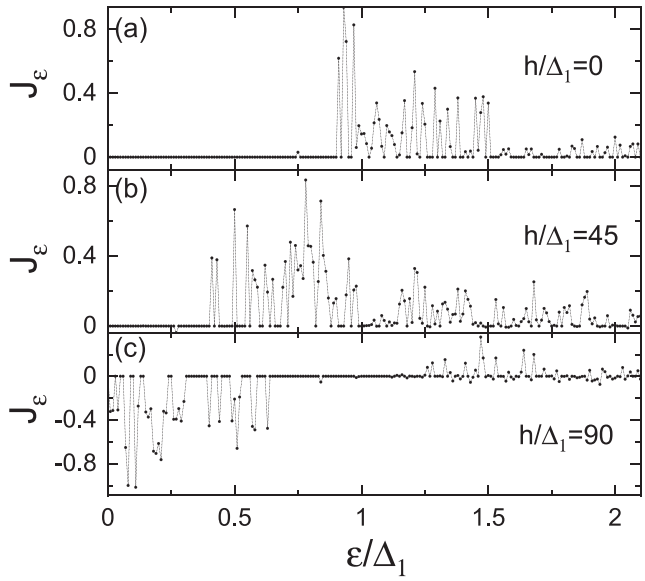

FIG. 13. The energy-resolved supercurrent density J_ε for an S_1FS_2 junction with $\Delta_2/\Delta_1 = 5$ and Fermi level mismatch $\Lambda = 3$. Three different values of the normalized exchange energy h/Δ_1 are considered: (a) $h/\Delta_1 = 0$, (b) $h/\Delta_1 = 45$, and (c) $h/\Delta_1 = 90$. The macroscopic phase difference chosen in each case corresponds to $\Delta\varphi_c$, where $\Delta\varphi_c$ is the phase angle that leads to the largest magnitude of the total supercurrent. In panels (a) and (b) $\Delta\varphi_c = 106^\circ$, and for (c) we have $\Delta\varphi_c = 125^\circ$.

$\epsilon_\perp$ [see Eq. (2)]. To isolate the supercurrent contribution at supergap and subgap energies, it is beneficial to extract the supercurrent response as a function of the quasiparticle energy ϵ. This procedure involves calculating the supercurrent for each quasiparticle trajectory with associated energy $\epsilon_\perp$. All trajectories are then summed over to arrive at the supercurrent for a given energy.

This procedure gives the results shown in Fig. 12, where the supercurrent is mapped out as a function of energy and phase difference. For concreteness, we take the parameters used in Figs. 8(a)–8(d), where a broad range of gap asymmetries were considered. Note the emergence of the J_2 supercurrent in the current phase relations can be accounted for in Figs. 12(b)–12(d) where the current carrying states get shifted upwards into the supergap region and broaden with increased Δ_2/Δ_1. This also leads to an amplification of the J_2 component and in turn the total supercurrent.

The energy-resolved supercurrent for an asymmetric Josephson junction at fixed phase is shown in Fig. 13. We take a relative ratio of $\Delta_2/\Delta_1 = 5$ and mismatch in Fermi levels corresponding to $\Lambda = 3$. Figure 13(a) corresponds to a nonmagnetic junction while Figs. 13(b) and 13(c) describe a ferromagnetic junction with differing exchange field strengths, as shown. For consistency, these system parameters correlate with Fig. 5(g). To correlate with the critical current components, from Fig. 5(g), it is seen that for $h/\Delta_1 = 0$ the supergap component J_2 dominates, while for $h/\Delta_1 = 90$, the subgap J_1 component does. The intermediate case of

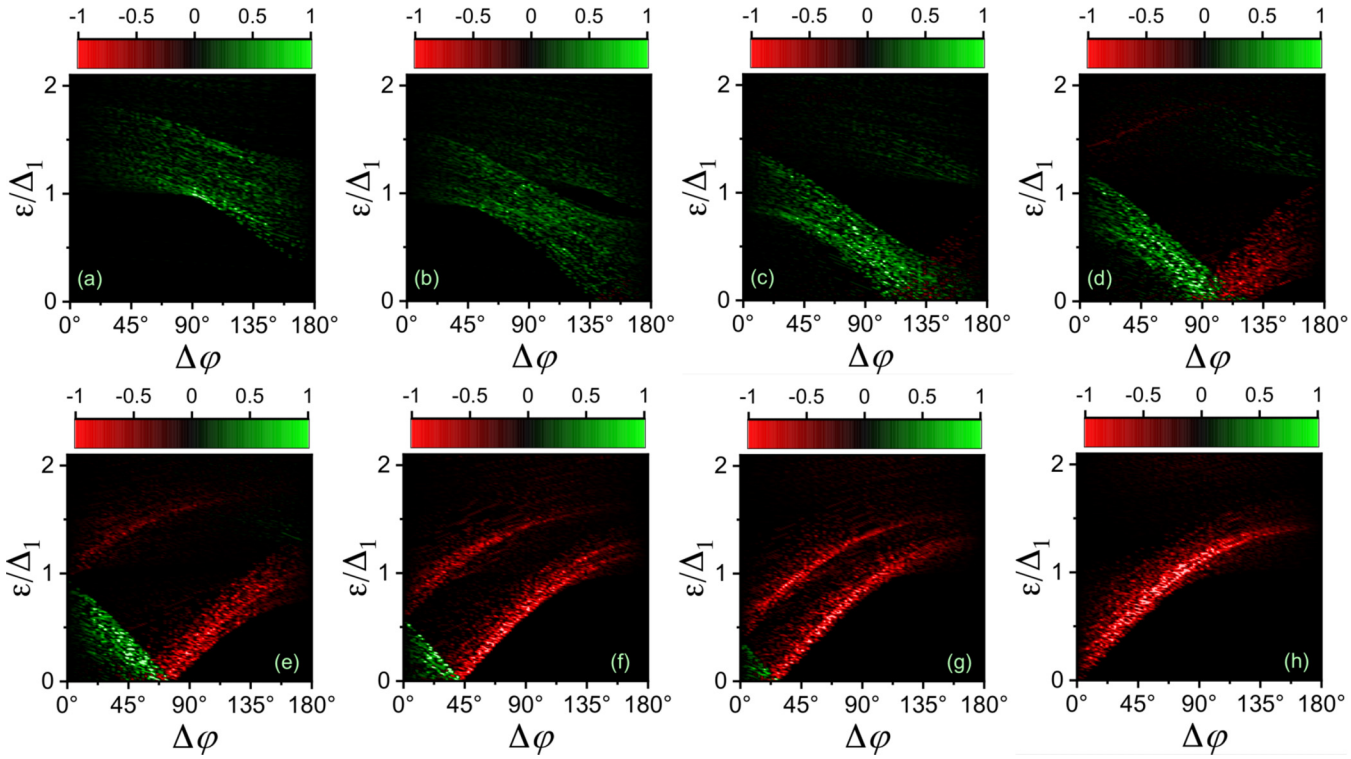

FIG. 14. Total supercurrent density mappings as a function of phase difference $\Delta\varphi$ and energy ε for an asymmetric Josephson junction with $\Delta_2/\Delta_1 = 5$. The Fermi level mismatch parameter is set to $\Lambda = 3$. Panels (a)–(h) depict differing normalized exchange fields h/Δ_1 corresponding to 0,45,70,90,110,130,140, and 160, respectively.

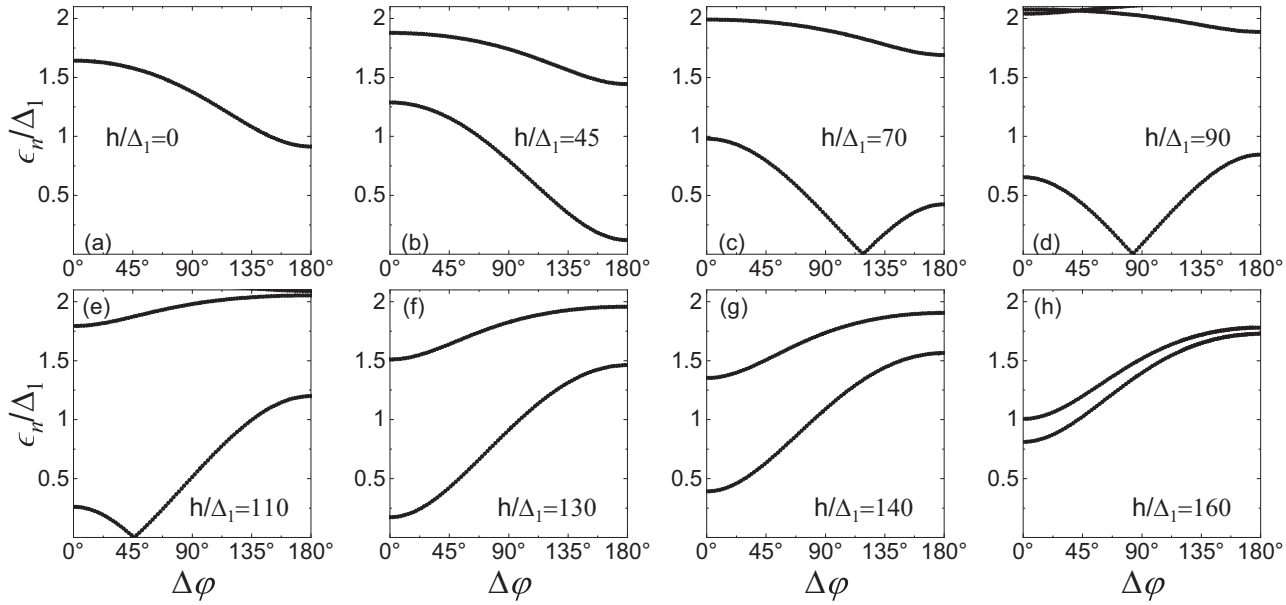

FIG. 15. The discrete energy spectrum for an asymmetric Josephson junction with $\Delta_2/\Delta_1 = 5$ and Fermi level mismatch corresponding to $\Lambda = 3$. The normalized exchange fields considered correlate with Fig. 14 above.

$h/\Delta_1 = 45$ has the subgap J_1 and supergap J_2 components contributing nearly equally to the critical current. This behavior is accounted for in the energy dependence of the supercurrent presented in Figs. 13(a)–13(c), where we take $\Delta\varphi = \Delta\varphi_c$ in each case to ensure that it gives the critical current shown in Fig. 5(g). The shift in current carrying states is evident as the exchange energy increases, until eventually reversing direction for $h/\Delta_1 = 90$ where the subgap bound states dominate.

To give a more comprehensive view of the energy-resolved supercurrent, we present in Fig. 14 the normalized supercurrent as a function of the normalized energy ϵ/Δ_1 and phase difference $\Delta\varphi$. Eight different exchange fields are considered, and the system parameters again coincide with the critical current study in Fig. 5(g). As seen in Figs. 14(a)–14(h), the supercurrent profiles exhibit varying amounts of mixtures between the subgap and supergap states. As the exchange field increases, the supercurrent flow evolves to contain states that have oppositely directed flow in both the subgap ($\epsilon \leqslant \Delta_1$) and supergap ($\Delta_1 \leqslant \epsilon \leqslant \Delta_2$) regions. Remarkably, increasing the exchange field can increase the supercurrent, including the half-metallic limit [Fig. 14(h)], where the supercurrent can exceed the supercurrent found in Fig. 14(a) for the nonmagnetic case. This can have important

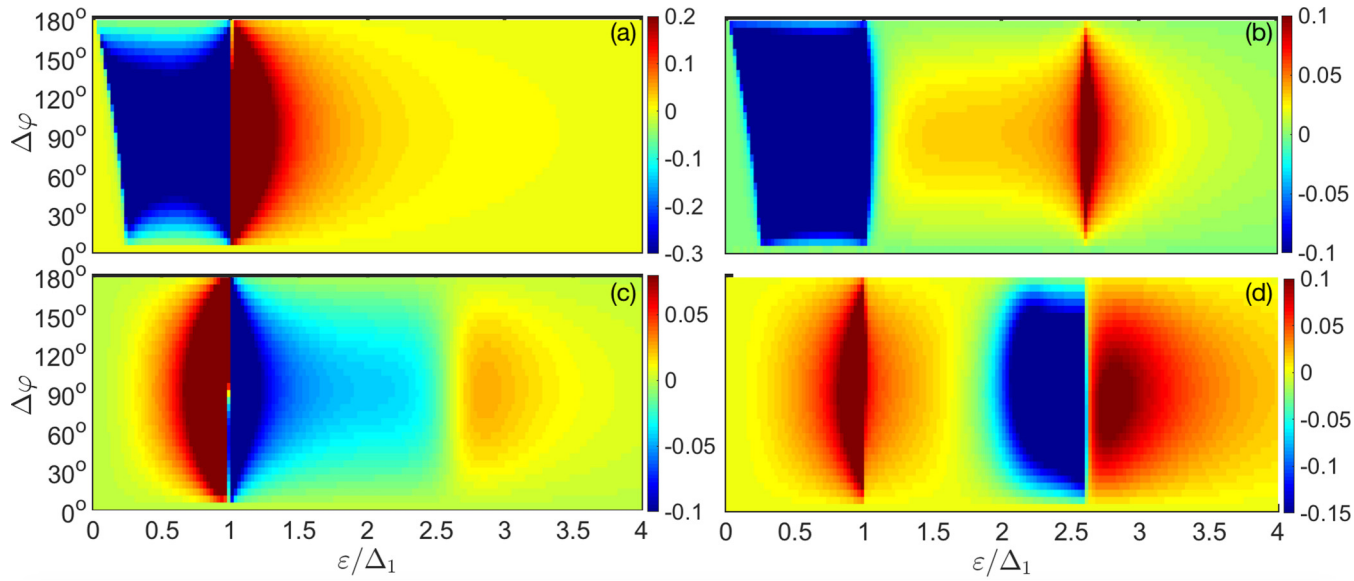

FIG. 16. Color map of the supercurrent density as a function of the normalized quasiparticle energy ε/Δ_1 and superconducting phase difference $\Delta\varphi$ in the diffusive regime. The junction parameter values are set in each panel to those of Fig. 11, except now we have (a) S_1NS_2: $h = 0$, $\Delta_2/\Delta_1 = 1$, (b) S_1NS_2: $h = 0$, $\Delta_2/\Delta_1 = 2.6$, (c) S_1FS_2: $h = 2.6\Delta_1$, $\Delta_2/\Delta_1 = 1$, and (d) S_1FS_2: $h = 2.6\Delta_1$, $\Delta_2/\Delta_1 = 2.6$.

consequences for devices that utilize the spin degree of freedom in Josephson junction systems. Note that the various admixtures of subgap and supergap supercurrents exhibited here can be directly correlated with the critical current signatures found in Fig. 5(g).

To delve further into the phase dependence of the supercurrent flow, we next present in Fig. 15 the quasiparticle energy spectra ϵ_n for each of the cases shown in Fig. 14. We consider the $\epsilon_\perp = 0$ mode, noting that many of the other transverse modes have similar behavior, and the cumulative effect serves to only broaden the overall supercurrent profile. From the diagrams, it is clear that the current vanishes at $\Delta\varphi = 0^\circ$ and $\Delta\varphi = 180^\circ$, where $\partial\epsilon_n/\partial(\Delta\varphi) = 0$. The cusps in the energy dispersion are consistent with Fig. 14, where the current at certain energies becomes reversed. We also find that as the exchange field h increases, the additional branches of the energy dispersion which emerge increase in separation before coalescing at high exchange fields. Thus, although the supercurrent is a cumulation of quasiparticle amplitudes and energies, the energy spectrum alone gives valuable insight into the transport properties of asymmetric Josephson junctions.

APPENDIX C: ENERGY-RESOLVED SUPERCURRENT DENSITY: DIFFUSIVE REGIME

When impurity scattering dominates, we turn to the diffusive regime. In Fig. 16, we show the supercurrent response as a function of macroscopic phase difference $\Delta\varphi$ and normalized energy ϵ/Δ_1. In Figs. 16(a) and 16(b), a nonmagnetic junction $h = 0$ is considered. In Fig. 16(a), the junction is symmetric $\Delta_2/\Delta_1 = 1$, while in Fig. 16(b), an asymmetric junction with $\Delta_2/\Delta_1 = 2.6$ is shown. The bottom set of panels corresponds to a weak ferromagnet junction with $h/\Delta_1 = 2.6$. For the nonmagnetic case, Figs. 16(a) and 16(b) show how the supercurrent with energies above the gap Δ_1 get shifted by an amount corresponding to the gap asymmetry $\Delta_2/\Delta_1 = 2.6$. In the bottom set of panels, the exchange field $h = 2.6\Delta_1$ introduces an additional energy scale that redistributes the supercurrent response. In the symmetric case Fig. 16(c) demonstrates how the presence of magnetism induces a supercurrent reversal for energies centered around the gap Δ_1. When the junction becomes asymmetric, the mutual effects of the exchange field and gap asymmetry lead to an enhancement of the supercurrent density at larger energies around Δ_2 [Fig. 16(d)].

[1] B. D. Josephson, Possible new effect in superconducting tunneling, Phys. Lett. **1**, 251 (1962).

[2] P. G. de Gennes, *Superconductivity of Metals and Alloys* (Addison-Wesley, Reading, MA, 1989).

[3] V. V. Ryazanov, V. A. Oboznov, A. V. Veretennikov, and A. Yu. Rusanov, Intrinsically frustrated superconducting array of superconductor-ferromagnet-superconductor π junctions, Phys. Rev. B **65**, 020501(R) (2001).

[4] V. V. Ryazanov, V. A. Oboznov, A. Yu. Rusanov, A. V. Veretennikov, A. A. Golubov, and J. Aarts, Coupling of Two Superconductors Through a Ferromagnet: Evidence For a π Junction, Phys. Rev. Lett. **86**, 2427 (2001).

[5] Z. Radovic, N. Lazarides, and N. Flytzanis, Josephson effect in double-barrier superconductor-ferromagnet junctions, Phys. Rev. B **68**, 014501 (2003).

[6] T. Kontos, M. Aprili, J. Lesueur, F. Genet, B. Stephanidis, and R. Boursier, Josephson Junction Through a Thin Ferromagnetic Layer: Negative Coupling, Phys. Rev. Lett. **89**, 137007 (2002).

[7] Ya. V. Fominov, A. F. Volkov, and K. B. Efetov, Josephson effect due to the long-range odd-frequency triplet superconductivity in junctions with Neel domain walls, Phys. Rev. B **75**, 104509 (2007).

[8] S. Takahashi, S. Hikino, M. Mori, J. Martinek, and S. Maekawa, Supercurrent Pumping in Josephson Junctions with a Half-Metallic Ferromagnet, Phys. Rev. Lett. **99**, 057003 (2007).

[9] K. Halterman and O. T. Valls, Layered ferromagnet-superconductor structures: The $0-\pi$ state and proximity effects, Phys. Rev. B **69**, 014517 (2004).

[10] K. Halterman and O. T. Valls, Proximity effects at ferromagnet-superconductor interfaces, Phys. Rev. B **65**, 014509 (2001).

[11] V. Shelukhin, A. Tsukernik, M. Karpovski, Y. Blum, K. B. Efetov, A. F. Volkov, T. Champel, M. Eschrig, T. Löfwander, G. Schön, and A. Palevski, Observation of periodic π-phase shifts in ferromagnet-superconductor multilayers, Phys. Rev. B **73**, 174506 (2006).

[12] T. Karabassov, A. V. Guravova, A. Yu. Kuzin, E. A. Kazakova, S. Kawabata, B. G. Lvov, and A. S. Vasenko, Anomalous current-voltage characteristics of SFIFS Josephson junctions with weak ferromagnetic interlayers, Beilstein J. Nanotechnol. **11**, 252 (2020).

[13] S. Acharjee and U. D. Goswami, Spin transport and spin tunnelling magneto-resistance (STMR) of F–NCSC–F spin valve, J. Mag. Mag. Mat. **495**, 165844 (2020).

[14] Z. Shomali, M. Zareyan, and W. Belzig, Spin supercurrent in Josephson contacts with noncollinear ferromagnets, New J. Phys. **13**, 083033 (2011).

[15] S. Hikino, Magnetization reversal by tuning Rashba spin–orbit interaction and Josephson phase in a ferromagnetic Josephson junction, J. Phys. Soc. Jpn. **87**, 074707 (2018).

[16] F. Setiawan, A. Stern, and E. Berg, Topological superconductivity in planar Josephson junctions: Narrowing down to the nanowire limit, Phys. Rev. B **99**, 220506(R) (2019).

[17] M. Alidoust and K. Halterman, Proximity induced vortices and long-range triplet supercurrents in ferromagnetic Josephson junctions and spin valves, J. Appl. Phys. **117**, 123906 (2015).

[18] E. Moen and O. T. Valls, Quasiparticle conductance in spin valve Josephson structures, Phys. Rev. B **101**, 184522 (2020).

[19] H. Chakraborti, S. Deb, R. Schott, V. Thakur, A. Chatterjee, S. Yadav, R. K. Saroj, A. Wieck, S. M. Shivaprasad, K. Das Gupta, and S. Dhar, Coherent transmission of superconducting carriers through a $\sim 2\ \mu$m polar semiconductor, Supercond. Sci. Technol. **31**, 085007 (2018).

[20] T. Karabassov, V. S. Stolyarov, A. A. Golubov, V. M. Silkin, V. M. Bayazitov, B. G. Lvov, and A. S. Vasenko, Competitive 0 and π states in S/F/S trilayers: Multimode approach, Phys. Rev. B **100**, 104502 (2019).

[21] S. V. Bakurskiy, A. A. Neilo, N. V. Klenov, I. I. Soloviev, and M. Yu. Kupriyanov, Dynamic properties of asymmetric double Josephson junction stack with quasiparticle imbalance, Nanotechnology **30**, 324004 (2019).

[22] Z. Shomali and R. Asgari, Spin transfer torque and exchange coupling in Josephson junctions with ferromagnetic superconductor reservoirs, J. Phys.: Condens. Matter **32**, 035806 (2020).

[23] M. V. Avdeev and Yu. N. Proshin, Long-range spin-singlet proximity effect for a Josephson system with a single-crystal ferromagnet due to its band-structure features, Phys. Rev. B **97**, 100502(R) (2018).

[24] E. Moen and O. T. Valls, Spin-split conductance and subgap peak in ferromagnet/superconductor spin valve heterostructures, Phys. Rev. B **98**, 104512 (2018).

[25] K. Ohnishi, S. Komori, G. Yang, K.-R. Jeon, L. A. B. Olde Olthof, X. Montiel, M. G. Blamire, and J. W. A. Robinson, Spin-transport in superconductors, Appl. Phys. Lett. **116**, 130501 (2020).

[26] K. Kulikov, D. Sinha, Yu. M. Shukrinov, and K. Sengupta, Josephson junctions of Weyl and multi-Weyl semimetals, Phys. Rev. B **101**, 075110 (2020).

[27] T. Vezin, C. Shen, J. E. Han, and I. Zutic, Enhanced spin-triplet pairing in magnetic junctions with s-wave superconductors, Phys. Rev. B **101**, 014515 (2020).

[28] A. Costa and J. Fabian, Anomalous Josephson Hall effect charge and transverse spin currents in superconductor/ferromagnetic-insulator/superconductor junctions, Phys. Rev. B **101**, 104508 (2020).

[29] A. A. Mazanik, I. R. Rahmonov, A. E. Botha, and Yu. M. Shukrinov, Analytical Criteria for Magnetization Reversal in a φ_0 Josephson Junction, Phys. Rev. Appl. **14**, 014003 (2020).

[30] H. Meng, Y. Ren, J. E. Villegas, and A. I. Buzdin, Josephson current through a ferromagnetic bilayer: Beyond the quasiclassical approximation, Phys. Rev. B **100**, 224514 (2019).

[31] C. W. J. Beenakker, Universal Limit of Critical-Current Fluctuations in Mesoscopic Josephson Junctions, Phys. Rev. Lett. **67**, 3836 (1991).

[32] E. Koshina and V. Krivoruchko, Spin polarization and π phase state of the Josephson contact: Critical current of mesoscopic SFIFS and SFIS junctions, Phys. Rev. B **63**, 224515 (2001).

[33] A. A. Golubov, M. Yu. Kupriyanov, and Ya. V. Fominov, Critical current in SFIFS junctions, Pis'ma Zh. Eksp. Teor. Fiz. **75**, 223 (2002) [JETP Lett. **75**, 190 (2002)].

[34] K. Halterman and O. T. Valls, Proximity effects and characteristic lengths in ferromagnet-superconductor structures, Phys. Rev. B **66**, 224516 (2002).

[35] M. Alidoust, Critical supercurrent and φ_0 state for probing a persistent spin helix, Phys. Rev. B **101**, 155123 (2020).

[36] K. Halterman, O. T. Valls, and C.-T. Wu, Charge and spin currents in ferromagnetic Josephson junctions, Phys. Rev. B **92**, 174516 (2015).

[37] C.-T. Wu and K. Halterman, Spin transport in half-metallic ferromagnet-superconductor junctions, Phys. Rev. B **98**, 054518 (2018).

[38] G. Tkachov, *Topological Insulators* (Taylor and Francis, Abingdon, 2016).

[39] A. V. Galaktionov, Supersymmetric Hamiltonian solutions simulated by Andreev bound states, Phys. Rev. B **101**, 134501 (2020).

[40] A. G. Golubov, M. Yu. Kupriyanov, and E. llichev, The current-phase relation in Josephson junctions, Rev. Mod. Phys. **76**, 411 (2004).

[41] A. Iovan and V. M. Krasnov, Signatures of the spin-triplet current in a Josephson spin valve: A micromagnetic analysis, Phys. Rev. B **96**, 014511 (2017).

[42] O. M. Kapran, A. Iovan, T. Golod, and V. M. Krasnov, Observation of the dominant spin-triplet supercurrent in Josephson spin valves with strong Ni ferromagnets, Phys. Rev. Research **2**, 013167 (2020).

[43] L. R. Tagirov, M. Yu. Kupriyanov, V. N. Kushnir, and A. Sidorenko, *Superconducting Triplet Proximity and Josephson Spin Valves*, Functional Nanostructures and Metamaterials for Superconducting Spintronics. NanoScience and Technology (Springer, Cham, 2018).

[44] D. Culcer, A. C. Keser, Y. Li, and G. Tkachov, Transport in two-dimensional topological materials: Recent developments in experiment and theory, 2D Mater. **7**, 022007 (2020).

[45] M. Alidoust, K. Halterman, and O. T. Valls, Zero-energy peak and triplet correlations in nanoscale SFF spin-valves, Phys. Rev. B **92**, 014508 (2015).

[46] K. Halterman and M. Alidoust, Half-metallic superconducting triplet spin valve, Phys. Rev. B **94**, 064503 (2016).

[47] A. Srivastava, L. A. B. Olde Olthof, A. Di Bernardo, S. Komori, M. Amado, C. Palomares-Garcia, M. Alidoust, K. Halterman, M. G. Blamire, and J. W. A. Robinsonn, Magnetization-Control And Transfer Of Spin-Polarized Cooper Pairs Into A Half-Metal Manganite, Phys. Rev. Appl. **8**, 044008 (2017).

[48] M. Alidoust and K. Halterman, Half-metallic superconducting triplet spin multivalve, Phys. Rev. B **97**, 064517 (2018).

[49] A. A. Abrikosov, L. P. Gorkov, and I. E. Dzyaloshinski, in *Methods of Quantum Field Theory in Statistical Physics*, edited by A. Silverman (Dover Publications, New York, 1963).

[50] G. Eilenberger, Transformation of Gorkov's equation for type-II superconductors into transport-like equations, Z. Phys. **214**, 195 (1968).

[51] K. D. Usadel, Generalized Diffusion Equation for Superconducting Alloys, Phys. Rev. Lett. **25**, 507 (1970).

[52] M. Alidoust and K. Halterman, Spontaneous edge accumulation of spin currents in finite-size two-dimensional diffusive spin–orbit coupled SFS heterostructures, New J. Phys. **17**, 033001 (2015).

[53] M. Alidoust and K. Halterman, Long-range spin-triplet correlations and edge spin currents in diffusive spin–orbit coupled SNS hybrids with a single spin-active interface, J. Phys: Condens. Matter **27**, 235301 (2015).

[54] A. Zyuzin, M. Alidoust, and D. Loss, Josephson junction through a disordered topological insulator with helical magnetization, Phys. Rev. B **93**, 214502 (2016).

[55] M. Alidoust and H. Hamzehpour, Spontaneous supercurrent and φ_0 phase shift parallel to magnetized topological insulator interfaces, Phys. Rev. B **96**, 165422 (2017).

[56] M. Alidoust, Self-biased current, magnetic interference response, and superconducting vortices in tilted Weyl semimetals with disorder, Phys. Rev. B **98**, 245418 (2018).

[57] M. Alidoust, M. Willatzen, and A.-P. Jauho, Fraunhofer response and supercurrent spin switching in black phosphorus with strain and disorder, Phys. Rev. B **98**, 184505 (2018).

[58] L. F. Chang and P. F. Bagwell, Ballistic Josephson-current flow through an asymmetric superconductor/normal-metal/superconductor junction, Phys. Rev. B **49**, 15853 (1994).

[59] M. Y. Kuprianov, Stationary properties of clean SNS sandwiches, Sov. J. Low Temp. Phys. **7**, 342 (1981).

[60] K. Halterman and M. Alidoust, Josephson currents and spin-transfer torques in ballistic SFSFS nanojunctions, Supercond. Sci. Technol. **29**, 055007 (2016).

[61] M. Alidoust, M. Willatzen, and A.-P. Jauho, Strain-engineered Majorana zero energy modes and φ_0 Josephson state in black phosphorus, Phys. Rev. B **98**, 085414 (2018).

[62] M. Alidoust and K. Halterman, Evolution of pair correlation symmetries and supercurrent reversal in tilted Weyl semimetals, Phys. Rev. B **101**, 035120 (2020).

[63] A. V. Zaitsev, Quasiclassical equations of the theory of superconductivity for contiguous metals and the properties of constricted microcontacts, Sov. Phys. JETP **59**, 1015 (1984); M. Y. Kuprianov and V. F. Lukichev, Influence of boundary transparency on the critical current of dirty SS'S structures, *ibid.* **67**, 1163 (1988).

[64] K. Halterman and O. T. Valls, Local density of states and order parameter configurations in layered ferromagnet-superconductor structures, Physica C **420**, 111 (2005).

[65] K. Halterman and O. T. Valls, Stability of π-junction configurations in ferromagnet-superconductor heterostructures, Phys. Rev. B **70**, 104516 (2004).

[66] K. Halterman and O. T. Valls, Energy gap of ferromagnet-superconductor bilayers, Physica C **397**, 151 (2003).

[67] A. I. Buzdin, L. N. Bulaevskii, and S. V. Panyukov, Critical-current oscillations as a function of the exchange field and thickness of the ferromagnetic metal (F) in an S-F-S Josephson junction, Pis'ma Zh. Eksp. Teor. Fiz. **35**, 147 (1982) [JETP Lett. **35**, 178 (1982)].

[68] O. Šipr and B. L. Györffy, Oscillatory magnetic coupling between metallic multilayers across superconducting spacers, J. Phys.: Condens. Matter **7**, 5239 (1995).